

Excitatory and inhibitory subnetworks are equally selective during decision-making and emerge simultaneously during learning

Farzaneh Najafi¹, Gamaleldin F Elsayed², Robin Cao³, Eftychios Pnevmatikakis⁴, Peter E. Latham³, John P Cunningham⁵, Anne K Churchland^{1,*}

¹Cold Spring Harbor Laboratory, Cold Spring Harbor, NY, ²Columbia University, Neuroscience, New York, NY, ³Gatsby Computational Neuroscience Unit, University College London, London, UK, ⁴Flatiron Institute, New York, NY, ⁵Columbia University, Statistics, New York, NY

*Correspondence: churchland@cshl.edu

Summary

Inhibitory neurons, which play a critical role in decision-making models, are often simplified as a single pool of non-selective neurons lacking connection specificity. This assumption is supported by observations in primary visual cortex: inhibitory neurons are broadly tuned in vivo, and show non-specific connectivity in slice. Selectivity of excitatory and inhibitory neurons within decision circuits, and hence the validity of decision-making models, is unknown. We simultaneously measured excitatory and inhibitory neurons in posterior parietal cortex of mice judging multisensory stimuli. Surprisingly, excitatory and inhibitory neurons were equally selective for the animal's choice, both at the single cell and population level. Further, both cell types exhibited similar changes in selectivity and temporal dynamics during learning, paralleling behavioral improvements. These observations, combined with modeling, argue against circuit architectures assuming non-selective inhibitory neurons. Instead, they argue for selective subnetworks of inhibitory and excitatory neurons that are shaped by experience to support expert decision-making.

Keywords

inhibitory neurons; excitatory neurons; decision-making models; learning; calcium imaging; posterior parietal cortex; decoding; stability; correlations; rate discrimination

1 Introduction

2 In many decisions, noisy evidence is accumulated over time to support a categorical choice. At
3 the neural level, there are a number of models that can implement evidence accumulation (Wang,
4 2002; Machens et al., 2005; Bogacz et al., 2006; Lo and Wang, 2006; Wong and Wang, 2006;
5 Beck et al., 2008; Lim and Goldman, 2013; Rustichini and Padoa-Schioppa, 2015; Mi et al.,
6 2017). Although these circuit models have successfully reproduced key characteristics of
7 behavioral and neural data during perceptual decision-making, their empirical evaluation has
8 been elusive, mainly due to the challenge of identifying inhibitory neurons reliably and in large
9 numbers in behaving animals. Inhibition, which constitutes an essential component of these
10 models, is usually provided by a single pool of inhibitory neurons receiving broad input from all
11 excitatory neurons (non-selective inhibition, Deneve et al., 1999; Wang, 2002; Mi et al., 2017).

12 The assumption of non-selective inhibition in theoretical models was, perhaps, motivated by
13 empirical studies that examined the connectivity and tuning of inhibitory and excitatory neurons.
14 Many studies in primary visual cortex report that inhibitory neurons have, on average, broader
15 tuning curves than excitatory neurons for visual stimulus features such as orientation (Sohya et
16 al., 2007; Niell and Stryker, 2008; Liu et al., 2009; Kerlin et al., 2010; Bock et al., 2011; Hofer et
17 al., 2011; Atallah et al., 2012; Chen et al., 2013; Znamenskiy et al., 2018), spatial frequency
18 (Niell and Stryker, 2008; Kerlin et al., 2010; Znamenskiy et al., 2018), and temporal frequency
19 (Znamenskiy et al., 2018). The broad tuning in inhibitory neurons has been mostly attributed to
20 their dense (Hofer et al., 2011; Packer and Yuste, 2011) and functionally unbiased inputs from
21 the surrounding excitatory neurons (Kerlin et al., 2010; Bock et al., 2011; Hofer et al., 2011).
22 This is in contrast to excitatory neurons, which show relatively sharp selectivity to stimulus
23 features (Sohya et al., 2007; Niell and Stryker, 2008; Ch'ng and Reid, 2010; Kerlin et al., 2010;
24 Hofer et al., 2011; Isaacson and Scanziani, 2011; Lee et al., 2016), reflecting their specific and
25 non-random connectivity (Yoshimura et al., 2005; Ch'ng and Reid, 2010; Hofer et al., 2011; Ko
26 et al., 2011; Cossell et al., 2015; Ringach et al., 2016).

27 Based on the relatively weak tuning of inhibition, it seems reasonable to assume that inhibition in
28 decision circuits is non-specific. However, the overall picture from experimental observations is
29 more nuanced than the original studies would suggest. First, a number of V1 studies report
30 tuning of inhibitory neurons that is on par with excitatory neurons (Ma et al., 2010; Runyan et
31 al., 2010), likely supported by targeted connectivity with excitatory neurons (Yoshimura and
32 Callaway, 2005). Strong tuning of inhibitory neurons has also been reported in primary auditory
33 cortex (Moore and Wehr, 2013). Further, interneurons have been shown to selectively represent
34 key task parameters in behaving animals in areas beyond sensory cortices. In frontal and parietal
35 areas, interneurons can distinguish go vs. no-go responses (For example, Allen et al., 2017) as
36 well as the trial outcome (Pinto and Dan, 2015). Similarly, in the hippocampus, interneurons
37 have strong selectivity for the stimulus (Lowett-Brown 2017), and the animal's location (Maurer
38 et al., 2006; Ego-Stengel and Wilson, 2007).

39 This selectivity of inhibitory neurons in a wealth of areas and conditions argue that the
40 assumption of non-selective interneurons in decision-making models must be revisited. Here, we
41 aimed to evaluate this assumption directly. We compared the selectivity of inhibitory and
42 excitatory neurons in posterior parietal cortex (PPC) of mice during rate discrimination

43 decisions. Surprisingly, we found that excitatory and inhibitory neurons in PPC are equally
44 choice-selective. Our modeling argued that these observations support selective connections
45 between excitatory and inhibitory neurons, a network architecture that supports enhanced
46 decoding in the presence of noise. Finally, during learning, the specificity of excitatory and
47 inhibitory neurons increased in parallel. These results constrain decision-making models, and in
48 particular argue that in decision areas, subnetworks of selective inhibitory neurons emerge
49 during learning, and are engaged during expert decisions.

50 **Results**

51 To test how excitatory and inhibitory neurons coordinate during decision-making, we measured
52 neural activity in transgenic mice trained to report decisions about the repetition rate of a
53 sequence of multisensory events by licking to a left or right waterspout (Figure 1A; Figure S1A).
54 Trials consisted of simultaneous clicks and flashes, generated randomly (via a Poisson process)
55 at rates that ranged from 5 to 27 Hz over a 1000 ms period (Brunton et al., 2013; Odoemene et
56 al., 2017). Mice reported whether event rates were high or low compared to a category boundary
57 (16 Hz) that they learned from experience. Decisions depended strongly on stimulus rate:
58 performance was at chance when the stimulus rate was at the category boundary, and was better
59 at rates further from the category boundary (Figure 1B). A logistic regression model
60 demonstrated that choice depends on the current stimulus strength, previous choice outcome
61 (Hwang et al., 2017), and the time elapsed since the previous trial (Figure S1B).

62 We imaged excitatory and inhibitory neural activity by injecting a viral vector containing the
63 calcium indicator GCaMP6f to layer 2/3 of mouse Posterior Parietal Cortex (PPC; 2mm posterior
64 to Bregma, 1.7mm lateral to midline (Harvey et al., 2012; Funamizu et al., 2016; Goard et al.,
65 2016; Morcos and Harvey, 2016; Hwang et al., 2017; Song et al., 2017)). Mice expressed the red
66 fluorescent protein tdTomato transgenically in all GABAergic inhibitory neurons. We used a
67 two-channel two-photon microscope to record the activity of all neurons, a subset of which were
68 identified as inhibitory (Figure 1C). This allowed us to measure the activity of excitatory and
69 inhibitory populations in the same animal.

70 To detect neurons and extract calcium signals from imaging data, we leveraged an algorithm that
71 simultaneously identifies neurons, de-noises the fluorescence signal and de-mixes signals from
72 spatially overlapping components (Pnevmatikakis et al., 2016; Giovannucci et al., 2018) (Figure
73 1D middle). The algorithm also estimates spiking activity for each neuron, yielding, for each
74 frame, a number that is related to the spiking activity during that frame (Figure 1D right). We
75 refer to this number as “inferred spiking activity”, acknowledging that estimating spikes from
76 calcium signals is challenging (Chen et al., 2013). Analyses were performed on inferred spiking
77 activity. To identify inhibitory neurons, we used a method that we developed to correct for
78 bleed-through from the green to the red channel (Methods). We identified a subset of GCaMP6f-
79 expressing neurons as inhibitory neurons based on the signal intensity on the red channel as well
80 as the spatial correlation between red and green channels (Figure 1C right, cyan circles).
81 Inhibitory neurons constituted 11% of the population, within the range of the previous reports
82 (Beaulieu, 1993; Gabbott et al., 1997; Rudy et al., 2011; Sahara et al., 2012), but on the lower
83 side due to our desire to be conservative in assigning neurons to the inhibitory pool (Methods).

84

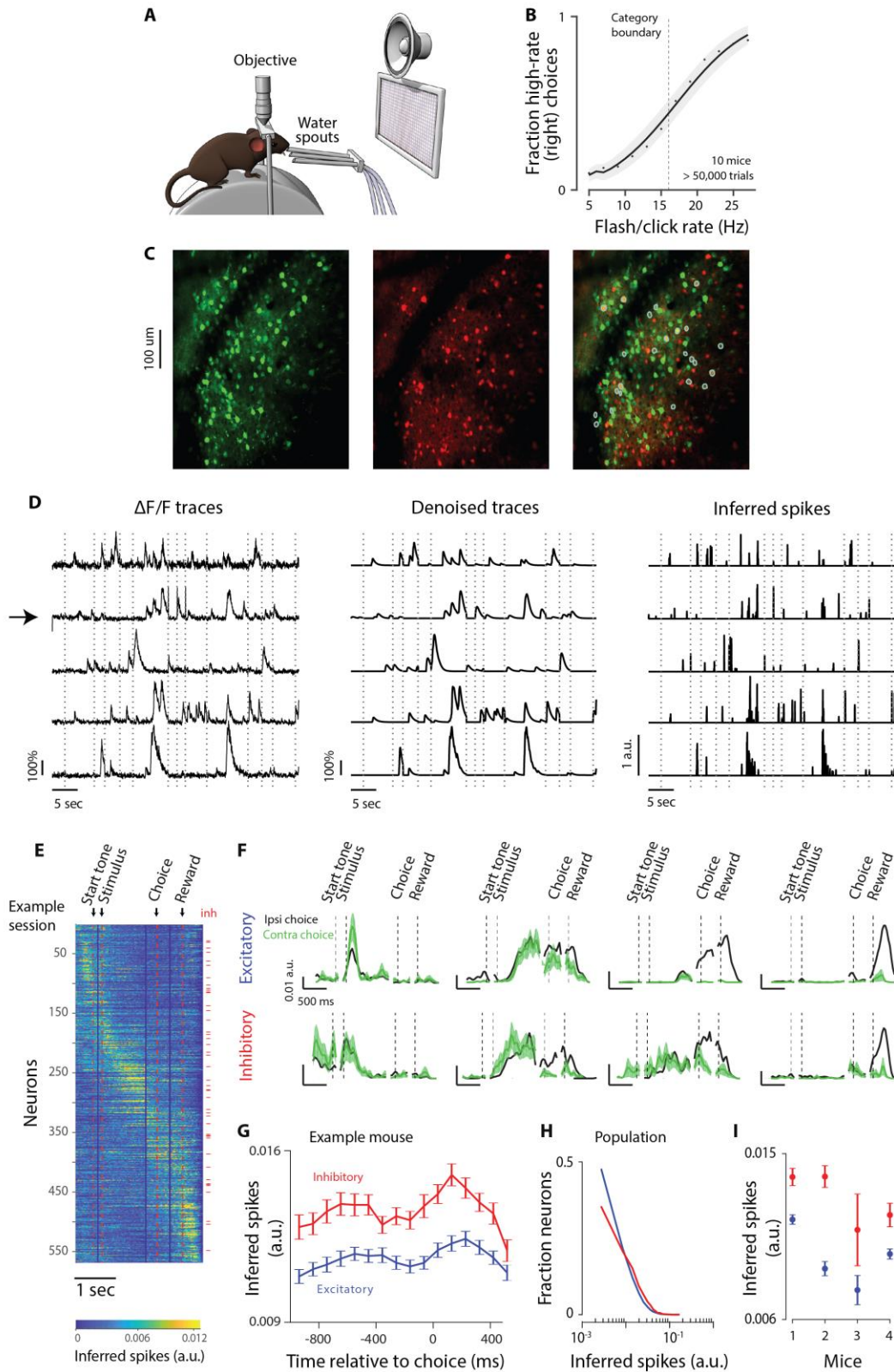


Figure 1. Simultaneous imaging of inhibitory and excitatory populations during decision-making.

A. Behavioral apparatus in which a head-fixed mouse is atop a cylindrical wheel. Multisensory stimuli are presented via a visual display and a speaker. To initiate a trial, mice lick the middle waterspout. To report the decision about the stimulus rate, mice lick left/right spouts. Objective belongs to the 2-photon microscope used to image neural activity through a window implanted in the skull. **B.** Psychometric function showing the fraction of trials in which the mouse judged the stimulus as high rate as a function of stimulus rate. Dots: data, mean across 10 mice. Line: Logit regression model fit using `glmfit.m`; mean across mice. Shaded area: standard deviation of the fit across mice. Dashed vertical line: category boundary (16Hz). **C.** Average image of 10,000 frames. **Left:** green channel showing GCaMP6f expression. **Middle:** red channel showing tdTomato expression. **Right:** merge of left and middle. Cyan circles indicate GCaMP6f-expressing neurons that were identified as inhibitory. **D.** Five example neurons identified by the Constrained Nonnegative Matrix Factorization algorithm (Methods) (arrow: inhibitory neuron). **Left:** raw $\Delta F/F$ traces. **Middle:** de-noised traces. **Right:** inferred spiking activity. Imaging was not performed during inter-trial intervals; traces from 13 consecutive trials are concatenated; dashed lines: trial onsets. **E.** Example session with 568 neurons. Each row shows the trial-averaged inferred spiking activity of a neuron (frame resolution: 32.4ms). Neurons are sorted according to the timing of their peak activity. To ensure peaks were not driven simply by noisy fluctuations, we first computed trial-averaged activity using half of the trials for each neuron. We then identified the time of peak activity for the trial-averaged response. Finally, these peak times were used to determine the plotting order for the trial-averaged activity corresponding to the remaining half of the trials. This cross-validated approach ensured that the tiling appearance of peak activities was not due to the combination of sorting and false-color-plotting. Inhibitory neurons ($n=45$) are indicated by red ticks on the right. Red vertical lines mark trial events: initiation (start) tone, stimulus onset, choice, and reward. Duration between events (e.g. between start tone and stimulus) varied across trials; so in order to make trial-averaged traces that represent how neural activity changes following trial events (e.g. start tone, stimulus, etc), traces were separately aligned to each trial event, and then averaged across trials. Next, these averaged traces (each aligned to a different trial event) were concatenated to represent neural activity during the entire trial duration, and in response to different trial events. Vertical blue lines indicate the border between the concatenated traces. **F.** Trial-averaged inferred spiking activity of 4 excitatory (top) and 4 inhibitory (bottom) neurons, for ipsi- (black) and contralateral (green) choices (mean +/- standard error; ~250 trials per session). **G.** Inferred spiking activity for excitatory (blue) and inhibitory (red) neurons during the course of a trial. Example mouse; mean +/- standard error across days ($n=46$). Each point corresponds to an average over trials and neurons. Inferred spiking activity was downsampled by averaging over three adjacent frames (Methods). This quantity was significantly higher for inhibitory neurons (t-test; $p<0.001$) at all times. **H.** Distribution of inferred spiking activity at time bin 0-97ms before the choice (averaged over three frames) for all mice and all sessions (41,723 excitatory and 5,142 inhibitory neurons). **I.** Inferred spiking activity at time bin 0-97ms before the choice (again, averaged over three frames) for each individual mouse (mean +/- standard error across days). Differences were significant for all subjects (t-test; $p<0.001$).

86 Confirming previous reports (Funamizu et al., 2016; Morcos and Harvey, 2016; Runyan et al.,
87 2017), we observed that the activity of individual neurons peaked at time points that spanned the
88 trial (Figure 1E,F). Diverse temporal dynamics were evident in both cell types (Figure 1E,F) and
89 did not appreciably differ between the two (Figure S2). The magnitude of inferred spiking
90 activity was significantly different for inhibitory compared to excitatory neurons throughout the
91 trial (Figure 1G; t-test, $p<0.001$). In the moments before the choice (97 ms, average of 3 frames),
92 this difference was clear (Figure 1H) and significant for all mice (Figure 1I). The probable
93 differences in GCaMP expression levels and calcium buffering between excitatory and inhibitory
94 neurons, as well as how spiking activity is inferred (Methods), makes a direct estimate of the
95 underlying firing rates challenging (Kwan and Dan, 2012). Nevertheless, the significant
96 difference in the inferred spiking activity between excitatory and inhibitory neurons provides
97 additional evidence that we successfully identified two separate neural populations.

98 **Individual excitatory and inhibitory neurons are similarly choice-selective**

99 To assess the selectivity of individual excitatory and inhibitory neurons for the decision outcome,
 100 we performed receiver operating characteristic (ROC) analysis (Green and Swets, 1966) on
 101 single-neuron responses. For each neuron, at each time point, we calculated the area under the
 102 ROC curve (AUC) as a measure of the amount of overlap between the response distributions for
 103 ipsilateral vs. contralateral choices. A neuron was identified as “choice-selective” if its AUC
 104 value was significantly different ($p < 0.05$) from a constructed shuffled distribution (Figure S3A;
 105 Methods), indicating that the neural activity was significantly different for ipsi- vs. contralateral
 106 choices (Figure 2A, shaded areas mark choice-selective neurons).

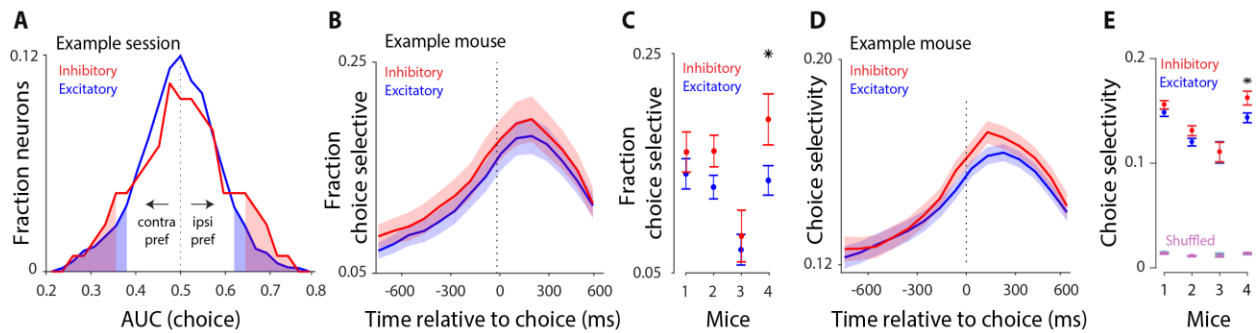


Figure 2. Single-cell and pairwise analyses argue for non-random connections between excitatory and inhibitory neurons.

Ideal observer analysis reveals the ability of individual neurons to distinguish left vs. right choices. In all panels, blue and red indicate excitatory and inhibitory neurons, respectively. **A**, Distribution of AUC values (area under the curve) of an ROC analysis for distinguishing choice from the activity of single neurons in an example session. Data correspond to the 97 ms window preceding the choice for 285 excitatory and 29 inhibitory neurons. Values larger than 0.5 indicate neurons preferring the ipsi-lateral choice; values smaller than 0.5 indicate neurons preferring the contralateral choice. Shaded areas mark significant AUC values (compared to a shuffle distribution). Distributions were smoothed (moving average, span=5). For this example session, 5 inhibitory and 24 excitatory neurons (17% and 8%, respectively) were significantly choice selective. **B**, ROC analysis performed on 97 ms non-overlapping time windows. Vertical axis: fraction of excitatory and inhibitory neurons with significant choice selectivity at the corresponding time on the horizontal axis; example mouse; mean \pm -standard error across days ($n = 45$ days). **C**, Fraction of excitatory and inhibitory neurons that are significantly choice-selective at 0-97 ms before the choice is summarized for each mouse; mean \pm -standard error across days ($n = 45, 48, 7, 35$ sessions per mouse). Star (*) indicates significant difference between excitatory and inhibitory neurons (t-test; $p < 0.05$); see also Figure S3D. Fraction selective neurons at 0-97ms before choice (median across mice): excitatory: 13%; inhibitory: 16%, resulting in ~6 inhibitory and 43 excitatory neurons with significant choice selectivity per session. See also Figure S3C for a different quantification. **D**, ROC analysis performed on 97 ms non-overlapping time windows. Time course of normalized choice selectivity (defined as twice the absolute deviation of AUC from chance, given explicitly by $2 \cdot |AUC - 0.5|$) shown for excitatory and inhibitory neurons in an example mouse; mean \pm -standard error across days, $n = 45$ sessions. **E**, Average of normalized choice selectivity for excitatory and inhibitory neurons from 0-97 ms before the choice is summarized for each mouse; mean \pm -standard error across days. “Shuffled” denotes AUC was computed using shuffled trial labels.

107 The fraction of choice-selective neurons (Figure 2B) and the magnitude of choice selectivity
 108 (Figure 2D) gradually increased during the course of the trial, peaking just after the animal
 109 reported its choice. Importantly, excitatory and inhibitory neurons were similar in terms of the
 110 fraction of choice-selective neurons (Figure 2B,C; Fig S3B,C), as well as the magnitude and time

111 course (Figure 2D,E) of choice selectivity. These results were not due to differences in inferred
112 spike rates of the two cell types (Figure 1G): when we restricted the ROC analysis to excitatory
113 and inhibitory neurons with similar spiking activity, both cell types remained equally selective
114 for the animal's choice (Figure S3D).

115 Next, we assessed whether neurons reflected the animal's choice or the sensory stimulus, by
116 comparing choice selectivity values resulting from ROC analysis performed on correct vs. error
117 trials. For the majority of neurons, choice selectivity computed on correct trials was similar to
118 that of error trials, resulting in a positive correlation of the two quantities across neurons (Figure
119 S3E). Positive correlations indicate that most neurons reflect the impending choice more so than
120 the sensory stimulus that informed it (Methods). Variability across mice in the strength of this
121 correlation may indicate that the balance of sensory vs. choice signals within individual neurons
122 varied across subjects (perhaps due to imaged subregions within the window, Figure S3E right).
123 Importantly, however, within each subject, this correlation was very similar for excitatory vs.
124 inhibitory neurons (Figure S3E), suggesting that within each animal, the tendency for neurons to
125 be modulated by the choice vs. the stimulus was similar in excitatory and inhibitory neurons.

126 The existence of task-modulated inhibitory neurons has been reported elsewhere (Maurer et al.,
127 2006; Ego-Stengel and Wilson, 2007; Lovett-Barron et al., 2014; Pinto and Dan, 2015; Allen et
128 al., 2017; Kamigaki and Dan, 2017), but importantly, here choice selectivity was similarly strong
129 in excitatory and inhibitory neurons, both in fraction and magnitude. This was at odds with the
130 commonly accepted assumption of non-specific inhibition in theoretical studies (Deneve et al.,
131 1999; Wang, 2002; Mi et al., 2017), and surprising given the numerous empirical findings, which
132 suggest broad tuning and weakly specific connectivity in inhibitory neurons (Sohya et al., 2007;
133 Niell and Stryker, 2008; Liu et al., 2009; Kerlin et al., 2010; Bock et al., 2011; Hofer et al., 2011;
134 Isaacson and Scanziani, 2011; Packer and Yuste, 2011; Atallah et al., 2012; Chen et al., 2013).
135 This observation was a first hint that specific functional subnetworks, preferring either ipsi- or
136 contralateral choices, exist within the inhibitory population, just like the excitatory population
137 (Yoshimura and Callaway, 2005; Znamenskiy et al., 2018).

138 **Choice can be decoded with equal accuracy from both excitatory and inhibitory** 139 **populations**

140 While individual inhibitory neurons could distinguish the animal's choice about as well as
141 excitatory ones, the overall choice selectivity in single neurons was small (Figure 2E). To further
142 evaluate the discrimination ability of inhibitory neurons, we leveraged our ability to record from
143 hundreds of neurons simultaneously. Specifically, we examined the ability of a linear classifier
144 (support vector machine, SVM; Hofmann et al., 2008) to predict the animal's choice from the
145 single-trial population activity (cross-validated; L2 penalty; see Methods).

146 We first performed this analysis on all neurons imaged simultaneously in a single session (Figure
147 3A, left), training the classifier separately for every moment in the trial (97 ms bins).
148 Classification accuracy gradually grew after stimulus onset and peaked at the time of the choice
149 (Figure 3B, black). Performance was at chance on a shuffle control in which trials were
150 randomly assigned as left or right choice (Figure 3B, shuffled). The ability of the entire
151 population of PPC neurons to predict the animal's upcoming choice confirms previous
152 observations (Funamizu et al., 2016; Goard et al., 2016; Morcos and Harvey, 2016; Driscoll et

153 al., 2017). Our overall classification accuracy was in the same range as these studies, and, as in
 154 those studies, was high despite the fact that many individual neurons in the population were only
 155 weakly selective (Fig. 2A).

156

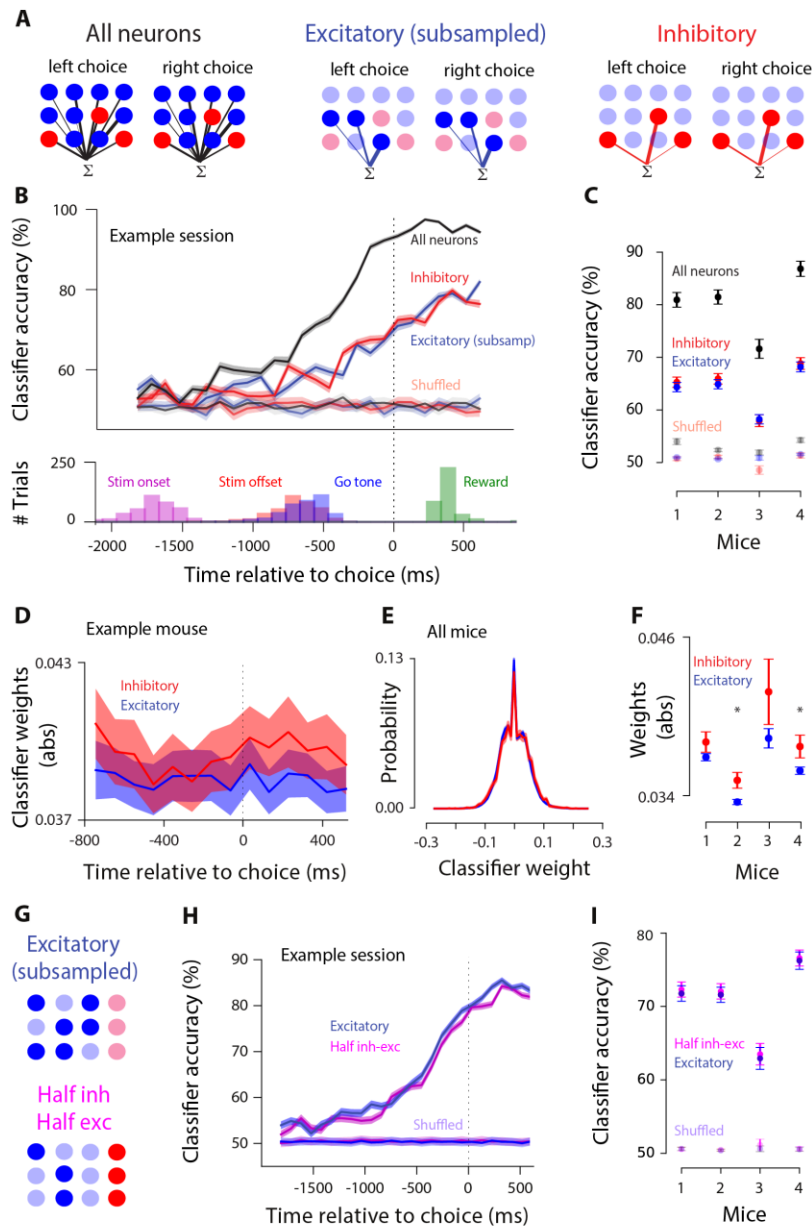


Figure 3. Linear classifiers can predict the animal's choice with equally high accuracy from the activity of either excitatory or inhibitory populations.

A, Schematic of decoding choice from the population activity of all neurons (left), only excitatory neurons (middle), subsampled to the same number as inhibitory neurons, and only inhibitory neurons (right). A linear SVM assigns weights of different magnitude (indicated by lines of different thickness) to each neuron in the population so that a weighted sum of population activity differs for trials preceding left vs. right choices. **B, Top**: classification accuracy of decoders trained on all neurons (black), subsampled excitatory neurons (blue), and inhibitory neurons (red) (cross-validated; decoders trained on every 97ms time bin; example session; mean \pm standard error across 50 cross-validated samples). Data are aligned to the animal's choice (black dotted line). Classification accuracy is lower for inhibitory or subsampled excitatory populations (red, blue) relative to all neurons (black) because of the smaller population size. Classifier accuracy was similar for excitatory and inhibitory populations throughout the trial. Unsaturated lines show performance on shuffled trial labels.

Bottom: distribution of stimulus onset, stimulus offset, go tone, and reward occurrence for the example session shown on the top. **C**, Classification accuracy during 0-97 ms before the choice for 4 animals on real (saturated) and shuffled (unsaturated) data. Mean \pm standard error across days per mouse. **D-F**, When all neurons were included in the decoder (panel A, left), excitatory and inhibitory neurons were assigned weights of similar magnitude. **D**, Absolute value of weights for excitatory and inhibitory neurons in the decoders trained on all neurons, at every moment in the trial; example mouse; mean \pm standard error across days. **E**, Distribution of classifier weights (decoder training time: 0-97 ms before the choice) are similar for excitatory and inhibitory neurons. Neurons from all mice pooled (42,019 excitatory and 5,172 inhibitory neurons). Shading reflects the standard error in each bin of the distribution. **F**, Absolute value of weights in the classifier trained from 0-97 ms before the choice for excitatory vs. inhibitory neurons, for each mouse. Mean \pm standard error across days. Star indicates $P < 0.05$, t-test. **G**, Schematic of decoding choice from a population of subsampled excitatory neurons (top) vs. a population of the same size but including half inhibitory and half excitatory neurons (bottom). **H**, Classifier accuracy of populations including only excitatory (blue) or half inhibitory, half excitatory neurons (magenta); example session. Classifier trained at each moment in the trial. Traces show mean \pm standard error across 50 cross-validated samples. **I**, Summary of each mouse (mean \pm standard error across days) for the decoders trained from 0-97 ms before the choice.

157 We then examined classifier accuracy for excitatory and inhibitory populations separately. For
158 excitatory neurons, we subsampled the population so that the total number of neurons matched
159 the number of inhibitory neurons in the same session (Figure 3A, middle). As expected, overall
160 classification accuracy was reduced due to the smaller population size; although performance
161 was still well above chance and the temporal dynamics were the same as when all neurons were
162 included (Figure 3B, blue trace). Finally, we included all inhibitory neurons (Figure 3A, right).
163 The classification accuracy of inhibitory neurons was not only well above chance, but, moreover,
164 was very similar to that of excitatory neurons (Figure 3B, red and blue traces overlap; Figure S4:
165 additional example sessions). Similar classification accuracy for excitatory and inhibitory
166 populations was observed in all subjects (Figure 3C). This result was not due to using inferred
167 spikes: excitatory and inhibitory populations were equally choice selective even when the
168 decoding analysis was performed on raw calcium traces (Figure S5).

169 Our analysis may have obscured a difference between excitatory and inhibitory neurons because
170 it evaluated their performance separately, rather than considering how these neurons are
171 leveraged collectively in a classifier that can take advantage of both cell types. To test this, we
172 examined the classifier that was trained on all neurons (Figure 3A left; Figure 3B black), and
173 compared the classifier weights assigned to excitatory vs. inhibitory neurons. We found that the
174 weight magnitudes of excitatory and inhibitory neurons were matched for the entire course of the
175 trial (Figure 3D), and the distributions of weights was very similar (Figures 3E, F). The
176 comparable classifier weights for excitatory and inhibitory neurons are consistent with the
177 conclusion that both cell types were similarly informative about the animal's upcoming choice.

178 We next tested whether excitatory and inhibitory populations can be decoded more accurately
179 from a mixed population. This could occur, for example, if the excitatory-inhibitory correlations
180 were weak relative to excitatory-excitatory and inhibitory-inhibitory correlations (Panzeri et al.,
181 1999; Averbeck et al., 2006; Moreno-Bote et al., 2014). To assess this, we trained the classifier
182 on a population that included half excitatory and half inhibitory neurons (Figure 3G bottom), and
183 compared its choice-prediction accuracy with the classifier that was trained on a population of
184 the same size, but consisted only of excitatory neurons (Figure 3G top). We found similar

185 classification accuracy for both decoders during the entire trial (Figure 3H,I), arguing that a
 186 mixed population offers no major advantage to decoding.

187 We next trained new classifiers to evaluate whether population activity reflected additional task
 188 features. First, the population activity was somewhat informative about previous trial choice
 189 (Figure S6A), in agreement with previous studies (Morcos and Harvey, 2016; Hwang et al.,
 190 2017; Akrami et al., 2018); but also see (Zhong et al., 2018). Excitatory and inhibitory
 191 populations were similarly selective for the animal's previous choice (Figure S6A). The
 192 population activity was also somewhat informative about whether the stimulus was above or
 193 below the category boundary (Figure S6B). Again, excitatory and inhibitory populations were
 194 similarly selective (Figure S6B). Finally, PPC population activity was strongly selective for the
 195 outcome of the trial (reward vs. lack of reward; Figure S6C). Excitatory and inhibitory neurons
 196 showed a small but consistent difference in the classifier accuracy after the reward was delivered
 197 (Figure S6C), indicating that once the reward is delivered, the network is operating in a different
 198 regime compared to during decision formation, perhaps due to distinct reward-related inputs to
 199 excitatory and inhibitory neurons (Pinto and Dan, 2015; Allen et al., 2017). This finding is
 200 broadly in keeping with previous studies which suggest that neural populations explore different
 201 dimensions over the course of a trial (Raposo et al., 2014; Elsayed et al., 2016).

202 Finally, we studied the temporal dynamics of the choice signal in PPC population during the
 203 course of the trial. If excitatory and inhibitory neurons are connected within subnetworks with

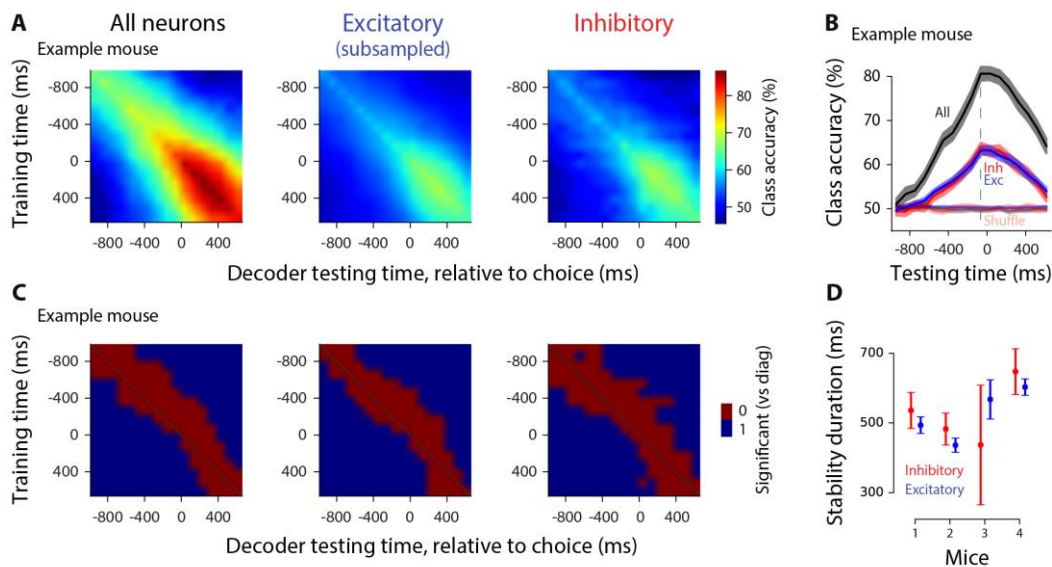


Figure 4. Classifiers, whether trained on excitatory or inhibitory neurons, show comparable stability during decision formation.

Cross-temporal generalization of choice decoders. **A**, Classification accuracy of decoders for each pair of training and testing time points, using the population activity of all neurons (left), subsampled excitatory neurons (middle), or inhibitory neurons (right). Diagonal: same training, testing time (same as in Figure 3). Example mouse, mean across 45 sessions. **B**, Example classification accuracy traces showing how classifiers trained at 0-97 ms before choice generalize to other times in the trial. Excitatory and inhibitory neurons show the same time course of generalization. Same mouse as in (A), mean \pm standard error across days. **C**, Decoders are stable in a short window outside their training time. Red indicates stability: classification accuracy of a decoder tested at a time different from its training time is within 2 standard deviations of the decoder tested at the same time as the training time. Example mouse; mean across days. **D**, Summary of stability duration for the decoder trained from 0-97 ms before the choice, using inhibitory neurons (red) or subsampled excitatory neurons (blue), for each mouse. Mean \pm standard error across days, per mouse.

204 frequent cross talk, the two populations should not only predict the animal's choice with similar
205 accuracy, as shown above, but the readout weights (the weights assigned by the classifier) should
206 exhibit similar temporal dynamics. To assess this, we quantified each population's stability: the
207 extent to which a classifier trained on choice at one moment could successfully classify choice at
208 different moments. If population-wide patterns of activity are similar over time (e.g., all neurons
209 gradually increase their firing rates), classifiers trained at one moment will accurately classify
210 neural activity at different moments. Excitatory and inhibitory populations might differ in this
211 regard, with one population more stable than the other.

212 As the gap between testing and training time increased, a gradual drop occurred in the classifier
213 accuracy, as expected (Figure 4A,B). This drop in accuracy occurred at a very similar rate for
214 excitatory and inhibitory populations (Figure 4B). To quantify this, we determined the time
215 window over which the classifier accuracy remained within 2 standard deviations of the accuracy
216 at the training window (Figure 4C). This was indistinguishable for excitatory and inhibitory
217 neurons (Figure 4D; Figure S7A). An alternate method for assessing stability, computing the
218 angle between the weights of pairs of classifiers trained at different time windows, likewise
219 suggested that excitatory and inhibitory populations are similarly stable (Methods; Figure S7C).

220 **Modeling rules out decision circuits with non-selective inhibition**

221 These results would seem to rule out circuitry from traditional decision-making models, in which
222 the inhibitory neurons are non-selective. This is because in non-selective circuits the average
223 input to the inhibitory neurons is the same whether the evidence favors choice 1 or choice 2 (see
224 Figure 5A, top). However, care must be taken in drawing this conclusion: while the average
225 input is the same, there are fluctuations in connection strength; those fluctuations will lead to at
226 least some selectivity in some inhibitory neurons. For instance, suppose that, because of the
227 inherent randomness in neural circuits, an inhibitory neuron received more connections from the
228 excitatory neurons in population E_1 than those in population E_2 . In that case, the firing rate of the
229 inhibitory neuron would be slightly higher when evidence in favor of choice 1 is present. That
230 difference in firing rate could potentially be exploited by a classifier to predict the choice of the
231 animal. Hence, one may argue that even a decision circuit with non-selective inhibition (Figure
232 5A, top) can lead to similar decoding accuracy in inhibitory and excitatory neurons, questioning
233 whether our experimental findings (Figures 2,3) can be leveraged to constrain decision-making
234 models.

235 To test this quantitatively, we modeled a non-selective circuit to evaluate the selectivity of
236 inhibitory neurons in such a circuit architecture (Methods). Classification accuracy depended on
237 the connection strengths between excitatory and inhibitory neurons (horizontal axis on Figure
238 5A, bottom), as those connection strengths affect overall activity in the network. The most
239 biologically plausible regime is near 0, corresponding to the equal strengths for excitatory-to-
240 inhibitory and inhibitory-to-excitatory connections (Thomson and Lamy, 2007; Jouhanneau et
241 al., 2015; Jouhanneau et al., 2018; Znamenskiy et al., 2018) (Figure 5A, arrow). For this value
242 (and indeed for all other values), inhibitory neurons had lower classification accuracy than
243 excitatory neurons (Figure 5A, bottom; Figure S8, left), inconsistent with our experimental
244 results (Figure 3B,C). Therefore, in the non-selective circuit, although some inhibitory neurons
245 can become selective due to random biased inputs from the excitatory pools, the classification

246 accuracy of inhibitory neurons will still be lower than excitatory neurons, regardless of the
 247 model parameters. This is because even modest amounts of noise in the system are sufficient to
 248 overcome any informative randomness in excitatory to inhibitory connections.

249 Next, we modeled a signal-selective circuit; in which inhibitory neurons were connected
 250 preferentially to one excitatory pool over the other (Figure 5B, top). In this circuit architecture,
 251 inhibitory and excitatory neurons had matched classification accuracy when the connection
 252 strength from excitatory to inhibitory neurons was about the same as the strength from inhibitory
 253 to excitatory (Figure 5B, bottom; Figure S8, middle).

254 Interestingly, a third circuit configuration likewise gave rise to excitatory and inhibitory neurons

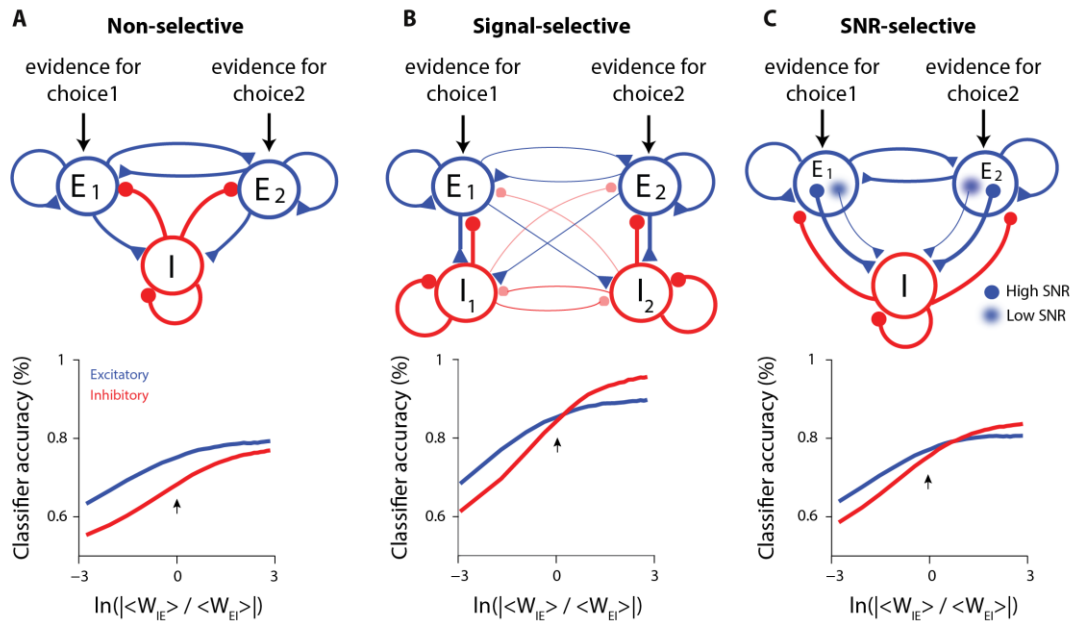


Figure 5. Modeling decision circuits with different architectures.

A, Top: Non-selective decision-making model. E_1 and E_2 represent pools of excitatory neurons, each favoring a different choice. Both pools excite a single pool of non-selective inhibitory neurons (I), which, in turn, provides inhibition to both excitatory pools. **Bottom:** Classification accuracy of excitatory (blue) and inhibitory (red) neurons as a function of the relative strength of excitatory-to-inhibitory vs. inhibitory-to-excitatory connections. For all values of this parameter, excitatory neurons had higher classification accuracy than inhibitory ones. This was true for all parameters tested (Methods; Figure S8; angle brackets denote averages over weights). The arrow in this and subsequent panels indicates the parameter value that is in line with experimental data, which suggest similar connectivity strength for E-to-I and I-to-E connections. **B, Top:** Selective decision-making model. I_1 and I_2 represent pools of inhibitory neurons that connect more strongly to E_1 and E_2 , respectively, than to E_2 and E_1 , and all cross-pool connections are weaker than within-pool connections. **Bottom:** Decoding accuracy of inhibitory and excitatory neurons match at the biologically plausible regime (arrow). Cross-pool connectivity was 25% smaller than within-pool connectivity. **C, Top:** Selective decision-making model, except now inhibitory neurons connect more strongly to excitatory neurons with high signal to noise ratios (i.e. high input selectivity). **Bottom:** Decoding accuracy of inhibitory and excitatory neurons match near the biologically plausible regime (arrow). In all panels, decoding accuracy depends on the relative strength of excitatory to inhibitory versus inhibitory to excitatory connections. In (B) and (C), larger excitatory to inhibitory connections favor inhibitory neurons. For all plots we used 50 excitatory and 50 inhibitory neurons out of a population containing 4000 excitatory and 1000 inhibitory neurons.

255 with matched classification accuracy near the biologically plausible regime (Figure 5C, bottom;
256 Figure S8, right). In this configuration, inhibitory neurons were non-selective with respect to the
257 excitatory pools, but were connected to the more selective excitatory neurons, i.e. those with a
258 high signal-to-noise ratio (Figure 5C, top).

259 Our modeling results raise two questions. First, how can the inhibitory neurons have better
260 decoding accuracy than the excitatory ones (Figure 5B,C, bottom; for part of the plot, red is
261 above blue)? After all, in our model all information about the choice flows through the excitatory
262 neurons. Second, why is the relative strength of the excitatory to inhibitory versus inhibitory to
263 excitatory connections an important parameter (Figure 5, bottom; x-axis)? The answers are
264 related. Increasing the strength of the excitatory to inhibitory connections increases the signal in
265 the inhibitory neurons, and therefore effectively decreases the noise added to the inhibitory
266 population (see Methods for details). This decrease in noise leads to improved decoding accuracy
267 of both the excitatory and inhibitory populations, because the two populations are connected.
268 However, the decrease in the noise added to the inhibitory neurons has a bigger effect on the
269 inhibitory than the excitatory population; that's because noise directly affects the inhibitory
270 neurons, but only indirectly, through the inhibitory to excitatory connections, affects the
271 excitatory neurons. Thus, in all panels of Figure 5, the classification accuracy increases faster for
272 inhibitory neurons than excitatory ones as the excitatory to inhibitory connection strength
273 increases. Interestingly, classification accuracy of both excitatory and inhibitory neurons was
274 overall higher for the signal-selective and SNR-selective models. This is because the selective
275 targeting of those models mitigates the noise that limits classification accuracy. This advantage
276 was most pronounced for the signal-selective model: the signal-selective model has significantly
277 higher classification accuracy compared to other models at all values of connectivity strength
278 and noise (Figure S9). This may indicate that the signal-selective network configuration is
279 especially advantageous to accurate decoding in the presence of noise.

280

281 Overall, our modeling work rules out decision circuits with non-selective inhibition (Figure 5A),
282 and instead demonstrates that excitatory and inhibitory neurons in decision circuits must be
283 selectively connected, either based on the signal preference (Figure 5B) or the informativeness
284 (Figure 5C) of excitatory neurons.

285 **Correlations are stronger between similarly tuned neurons**

286 We have demonstrated that inhibitory neurons are choice-selective (Figures 2,3). If choice
287 selectivity in inhibitory neurons emerges because of functionally biased input from excitatory
288 neurons, one prediction is that correlations will be stronger between excitatory and inhibitory
289 neurons with the same choice selectivity compared to those with the opposite choice selectivity
290 (Cossell et al., 2015; Francis et al., 2018). To test this hypothesis, we compared pairwise noise
291 correlations in the activity of neurons with the same vs. opposite choice selectivity (Methods).
292 Indeed, neurons with the same choice selectivity had stronger correlations (Figure 6A). This was
293 evident in pairs consisting of one excitatory, one inhibitory, only excitatory, or only inhibitory
294 neurons (Figure 6A, left to right), in keeping with previous observations in mouse V1 during
295 passive viewing (Hofer et al., 2011; Ko et al., 2011; Cossell et al., 2015; Znamenskiy et al.,

296 2018), as well as the prefrontal cortex in behaving monkeys (Constantinidis and Goldman-Rakic,
297 2002).

298 The higher noise correlations among similarly tuned excitatory-inhibitory neuron pairs is also
299 consistent with the observation that in V1, excitatory and inhibitory neurons that belong to the
300 same subnetwork are reciprocally connected (Yoshimura and Callaway, 2005). An alternative
301 explanation, that the neurons with similar tuning share common inputs, is also possible. **If that is**
302 **the case, however, the common input is not exclusively stimulus driven** because we observed the
303 same correlation effects in the pre-trial period in which there is no stimulus (Figure S10A).

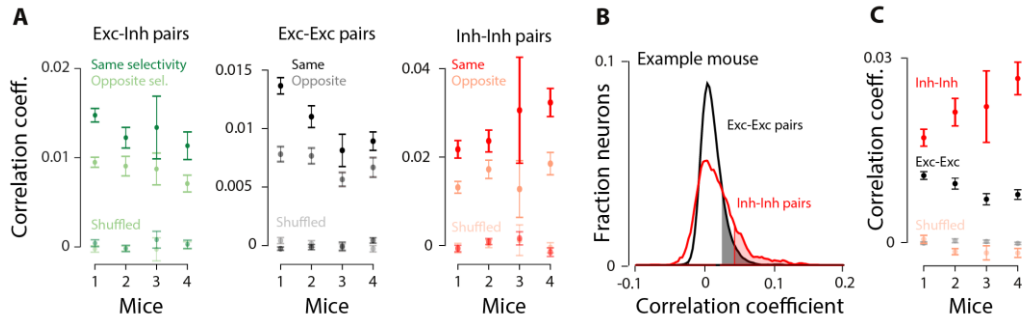


Figure 6. Pairwise noise correlations are stronger between neurons with the same choice selectivity.

A, Left: Noise correlations (Pearson's coefficient) for pairs of excitatory-inhibitory neurons with the same choice selectivity (dark green) or opposite choice selectivity (light green, i.e. one neuron prefers ipsilateral, and the other neuron prefers contralateral choice). **Middle, right:** same as in the left panel, but for excitatory-excitatory, and inhibitory-inhibitory pairs, respectively. "Shuffled" denotes quantities were computed using shuffled trial labels. Mean +/- standard error across days; 0-97 ms before the choice. Same vs. opposite is significant in all cases, except for mouse 3 in EE and II pairs (t-test, $p < 0.05$). **B,** Example mouse: distribution of noise correlations (Pearson's correlation coefficients, 0-97 ms before the choice) for excitatory neurons (blue; $n=11867$) and inhibitory neurons (red; $n=1583$). Shaded areas indicate significant quantities compared to a shuffled control in which trial orders were shuffled for each neuron to remove noise correlations. **C,** Summary of noise correlation coefficients for each mouse, indicating higher correlations among inhibitory neurons; mean +/- standard error across days.

304 We next compared the strength of pairwise noise correlations within our excitatory and
305 inhibitory populations. Inhibitory pairs had significantly higher noise correlations compared to
306 excitatory pairs (Figure 6B,C: noise correlations; Figure S10C: spontaneous correlations). We
307 obtained the same results even when we restricted the analysis to those inhibitory and excitatory
308 neurons that had the same inferred spiking activity (Figure S10D,E). This was done because the
309 higher spiking activity of inhibitory neurons (Figure 1G-I) could potentially muddle the
310 comparison of pairwise noise correlations between excitatory and inhibitory neurons. Finally,
311 similar to previous reports (Hofer et al., 2011; Khan et al., 2018), we found intermediate
312 correlations for pairs consisting of one inhibitory neuron and one excitatory neuron (Figure
313 S10B,C). These findings align with previous studies in sensory areas that have demonstrated
314 stronger correlations among inhibitory neurons (Hofer et al., 2011; Khan et al., 2018). These
315 correlations are likely driven at least in part by local connections, as evidenced by the dense
316 connectivity of interneurons with each other (Galarreta and Hestrin, 1999; Packer and Yuste,
317 2011; Kwan and Dan, 2012). The difference we observed between excitatory and inhibitory
318 neurons argues that this feature of early sensory circuits is shared by decision-making areas.

319 Further, this clear difference between excitatory and inhibitory neurons, like the difference in
320 inferred spiking (Figure 1G-I) and outcome selectivity (Figure S6C), confirms that we
321 successfully measured two distinct populations. Overall our noise correlation analysis suggests
322 that selective connectivity between excitatory and inhibitory neurons exist and depends on their
323 functional properties.

324 **Noise correlations limit decoding accuracy**

325 Our results thus far demonstrate that neural activities in both excitatory and inhibitory
326 populations reflect an animal's impending choice (Figure 3B,C), and that there are significant
327 noise correlations among neurons in PPC (Figure 6). However, the analyses so far do not
328 demonstrate how this noise affects the ability to decode neural activity overall, or for excitatory
329 and inhibitory populations separately. Examining the effect of noise is essential because
330 correlations affect the performance of classifiers (Panzeri et al., 1999; Averbeck et al., 2006),
331 with large effects possible even when correlations are weak (Averbeck et al., 2006; Moreno-Bote
332 et al., 2014). Fortunately, our dataset includes simultaneous activity from hundreds of neurons
333 and is therefore especially well-suited to assess noise correlations: correlations.

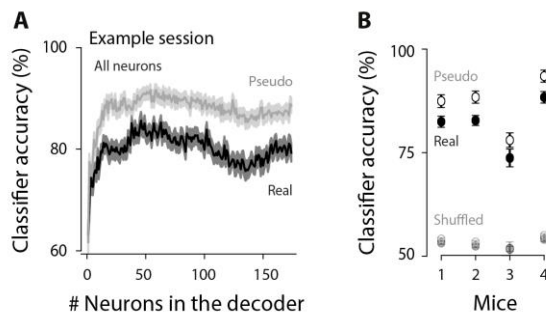


Figure 7. Noise correlations reduce classification accuracy.

A, Classification accuracy for an example session (at time window 0-97 ms before the choice) on neural ensembles of increasingly larger size, with the most choice-selective neurons added first. Mean \pm -standard error across 50 cross-validated samples. Gray: classification accuracy for pseudo-populations, in which noise correlations were removed by shuffling. Black: real populations. Both cell types were included (“All neurons”). **B**, Summary for each mouse; points show mean \pm -standard error across days. Values were computed for the largest neuronal ensemble (the max value on the horizontal axis in **A**).

334 To examine how noise correlations affect classification accuracy for choice, we sorted neurons
335 based on their individual choice selectivity, added them one by one to the population (from
336 highest to lowest choice selectivity defined as $|AUC-0.5|$), and measured classification accuracy
337 as a function of population size. Classification accuracy improved initially as more neurons were
338 included in the decoder, but quickly saturated (Figure 7A black; 0-97 ms before the choice).

339 To assess the role of noise correlations on classification accuracy, we created uncorrelated
340 “pseudo populations”, in which each neuron in the population was taken from a different trial
341 (Figure 7A gray). This removed noise correlations because those are shared across neurons
342 within a single trial. Higher classification accuracy in pseudo populations compared to real
343 populations indicates the presence of noise that overlaps with signal, limiting information
344 (Panzeri et al., 1999; Averbeck et al., 2006; Averbeck and Lee, 2006; Moreno-Bote et al., 2014).
345 This is what we observed (Figure 7A, gray trace above black trace). Across all mice, removing
346 noise correlations resulted in a consistent increase in classification accuracy for the full
347 population (Figure 7B; filled vs. open circles). This establishes that noise correlations reduce
348 population decoding in PPC.

349 **Selectivity increases in parallel in inhibitory and excitatory populations during learning**

350 Our observations thus far argue that excitatory and inhibitory neurons form selective
351 subnetworks. To assess whether the emergence of these subnetworks is experience-dependent,
352 and if it varies between inhibitory and excitatory populations, we measured neural activity as
353 animals transitioned from novice to expert decision-makers (3 mice; 35-48 sessions; Figure S11).
354 We trained a linear classifier for each training session, and for each moment in the trial. This
355 allowed us to compare the dynamics of the choice signal in excitatory and inhibitory populations
356 over the course of learning.

357 Classification accuracy of the choice decoder increased consistently as animals became experts
358 in decision-making (Figure 8A, left; Figure 8D, black), leading to a strong correlation between
359 the classifier performance and the animal's performance across training days (Figure 8B, left).
360 The population representation of the choice signal also became more prompt: the choice signal
361 appeared progressively earlier in the trial as the animals became experts. Initially, classification
362 accuracy was high only after the choice (Figure 8A, black arrow). As the animals gained
363 experience, high classification accuracy occurred progressively earlier in the trial, eventually
364 long before the choice (Figure 8A, gray arrow). This resulted in a negative correlation between
365 the animal's performance and the onset of super-threshold decoding accuracy relative to the
366 choice (Figure 8C, left; Figure 8E, black).

367 Importantly, the dynamics of the choice decoder changed in parallel in both excitatory and
368 inhibitory populations as a result of training: the choice signal emerged at the same time in both
369 populations, and its magnitude and timing was matched for the two cell types throughout
370 learning (Figure 8A-C, middle, right; Figure 8D-E, blue, red). This change was not due to the
371 presence of more correct trials in later sessions: an improvement in classification accuracy was
372 clear even when the number of correct trials was matched for each session (Figure S13C). These
373 findings indicate that learning induces the simultaneous emergence of choice-specific
374 subpopulations in excitatory and inhibitory cells in PPC.

375 Notably, the animal's licking or running behavior could not explain the learning-induced
376 changes in the magnitude of classification accuracy (Figure S12). The center-spout licks that
377 preceded the left vs. right choices were overall similar during the course of learning (Figure
378 S12A), and did not differ in early vs. late training days (Figure S12B). The similarity in lick
379 movements for early vs. late sessions stands in contrast to the changes in the classification
380 accuracy for early vs. late sessions (Figure 8). We also assessed animals' running behavior
381 during the course of learning (Figure S12C,D). In some sessions, the running distance differed
382 preceding left vs. right choices (Figure S12C). Nonetheless, when we restricted our analysis to
383 days in which the running distance was indistinguishable for the two choices (0-97 ms before the
384 choice, t-test, $P > 0.05$), we were still able to accurately classify the animal's choice using neural
385 activity (Figure S12D). These observations provide reassurance that the population activity does
386 not entirely reflect preparation of licking and running movements, and argue instead that the
387 population activity reflects the animal's stimulus-informed choice.

388 Finally, we studied how correlations changed over the course of training. Pairwise correlations in
389 neural activity were overall higher in early training days, when mice were novices, compared to
390 late training days, as they approached expert behavior (Figure 8F, unsaturated colors above

391 saturated colors). This effect was observed for all combinations of neural pairs (Figure 8F, green:
 392 excitatory-inhibitory; blue: excitatory-excitatory; red: inhibitory-inhibitory). These findings are
 393 in agreement with previous reports suggesting that learning results in reduced noise correlations

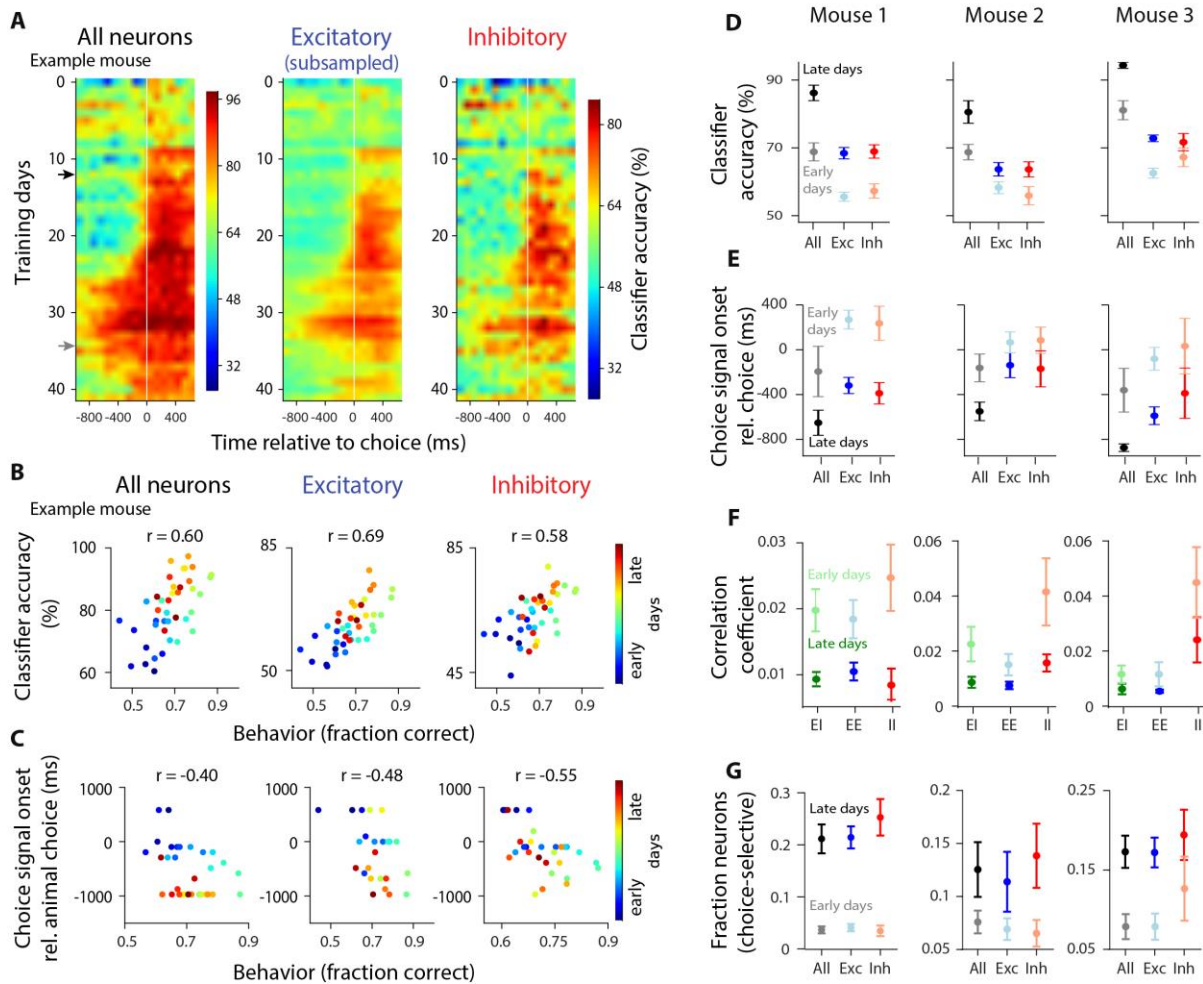


Figure 8. Learning leads to increased magnitude of the choice signal in the population, increased fraction of choice-selective neurons, and reduced noise correlations, in both excitatory and inhibitory populations.

A, Decoder accuracy for each training session, for all neurons (left), subsampled excitatory (middle), and inhibitory neurons (right). White vertical line: choice onset. Each row: average across cross-validation samples; example mouse. Colorbar of the inhibitory plot applies to the excitatory plot too. **B**, Scatter plot of classifier accuracy at 0-97 ms before the choice vs. behavioral performance (fraction correct on easy trials), including all training days. r is Pearson correlation coefficient ($p < 0.001$ in all plots); same example mouse as in (A). Correlations for behavior vs. classification accuracy for all neurons, excitatory and inhibitory: 0.55, 0.35, 0.32 in mouse 2; 0.57, 0.63, 0.32 in mouse 3. Correlations for behavior vs. choice-signal onset for all neurons, excitatory and inhibitory: -0.60, -0.34, -0.38, in mouse 2; -0.60, -0.27, -0.28 in mouse 3. All values: $p < 0.05$ **C**, Same as (B), except showing the onset of choice signal, i.e. the first moment in the trial that classifier accuracy was above chance (ms, relative to choice onset) vs. behavioral performance. **D**, Summary of each mouse, showing classification accuracy averaged across early (dim colors) vs. late (dark colors) training days. **E**, Same as (D), but showing choice signal onset (ms). **F**, Same as (D), but showing pairwise noise correlation coefficients. **G**, Fraction of choice-selective neurons increases as a result of training; average across early (dim colors) and late (dark colors) training days; time points 0-97 ms before the choice. Early days were the first few training days in which the animal's performance was lower than the 20th percentile of animal's performance across all days. Late days included the last training days in which the animal's behavioral performance was above the 80th percentile of performance across all days.

394 (Gu et al., 2011; Jeanne et al., 2013; Khan et al., 2018; Ni et al., 2018), enhancing information
395 that is encoded in neural populations. To test if the learning-induced increase in classification
396 accuracy (Figure 8A,B,D) was entirely a consequence of the reduction in noise correlations
397 (Figure 8F), we studied how classification accuracy of pseudo populations, which lack noise
398 correlations, changed with training. Interestingly, we still observed a significant increase in the
399 classification accuracy of pseudo populations as a result of training (Figure S13A,B). Therefore,
400 the reduction in noise correlations cannot alone account for the improved classification accuracy
401 that occurs during learning. Instead, it suggests that choice selectivity of individual neurons also
402 changes with learning. Indeed, the fraction of choice-selective neurons increased threefold, in
403 both excitatory and inhibitory cell types, as a result of training (Figure 8G), contributing to the
404 improved classification accuracy at the ensemble level.

405 **Discussion**

406 Despite a wealth of studies assessing the selectivity of inhibitory neurons in response to sensory
407 features, little is known about the selectivity of inhibitory neurons in decision-making. This
408 represents a critical gap in our knowledge, and has left untested key features of decision-making
409 models relying on inhibitory neurons. To close this gap, we simultaneously measured excitatory
410 and inhibitory populations during perceptual decisions about multisensory stimuli.

411 We demonstrated that excitatory and inhibitory neurons predict the animal's impending choice
412 with equal fidelity (Figure 2,3). This result, along with our modeling (Figure 5), constrains
413 circuit models of decision-making, ruling out models in which inhibitory neurons receive
414 completely nonspecific input from excitatory populations (Figure 5A). Instead, our findings
415 suggest that specific functional subnetworks exist within inhibitory populations, just like
416 excitatory populations (Figure 5B). This implies targeted connectivity between excitatory and
417 inhibitory neurons (Yoshimura and Callaway, 2005; Znamenskiy et al., 2018), and supports
418 circuit architectures with functionally specific subnetworks within excitatory and inhibitory
419 populations that are reciprocally connected.

420 [Why might signal selective architectures be present in decision-making circuits? A documented](#)
421 [advantage of signal-selective architectures is that they offer, at least in some regimes, improved](#)
422 [stability \(Znamenskiy et al., 2018\) and robustness to perturbations \(Lim and Goldman, 2013\).](#)
423 [However, in our circuit, selectivity did not improve stability, so we believe it instead offers](#)
424 [significantly improved performance: classification accuracy for the signal selective model was](#)
425 [the highest of the three we tested \(Figure 5B, bottom row, Figure S9\). Thus these observations](#)
426 [raise the possibility that among possible circuit architectures that could have been leveraged by](#)
427 [the brain to support decision-making, the highest-performing one was chosen.](#)

428 The equal selectivity for choice that we observed in excitatory and inhibitory populations is
429 perhaps, at first, surprising, given the broad stimulus tuning curves observed in most V1
430 inhibitory neurons (Sohya et al., 2007; Niell and Stryker, 2008; Kerlin et al., 2010; Bock et al.,
431 2011; Hofer et al., 2011; Znamenskiy et al., 2018) (but see Runyan et al., 2010) and the dense
432 connectivity for inhibitory neurons (Hofer et al., 2011; Packer and Yuste, 2011; Znamenskiy et
433 al., 2018) are often taken as evidence that inhibitory neurons are not strongly modulated by task
434 parameters. Two differences between our study and previous ones may explain why we saw
435 equal selectivity in excitatory and inhibitory populations.

436 First, we measured neural activity in PPC where the proportion of interneuron subtypes differ
437 from V1; in particular, early sensory areas are more enriched in PV interneurons relative to SOM
438 and VIP neurons, whereas the opposite is true in association areas (Kim et al., 2017; Wang and
439 Yang, 2018). Moreover, interneuron subtypes vary in their specificity of connections (Pfeffer et
440 al., 2013); for instance, PV interneurons are suggested to have broader tuning than SOM and VIP
441 cells (Wang et al., 2004; Ma et al., 2010). Therefore, the strong selectivity that we found in all
442 GABAergic interneurons in PPC may not contradict the broad selectivity observed in studies
443 largely performed on PV interneurons in V1. Future studies that measure the selectivity of
444 distinct interneuron populations during decision-making in V1 vs. PPC will be helpful. Here, we
445 measured all GABAergic interneurons instead of individual interneuron subtypes; this was
446 because of the technical challenges in reliably identifying more than two cell types in a single
447 animal, and because of the importance of simultaneously measuring the activity of excitatory and
448 inhibitory neurons within the same subject. Had we lacked within-animal measurements, our
449 ability to compare excitatory vs. inhibitory neurons would have been compromised by animal-to-
450 animal variability (e.g. note the matched selectivity of excitatory and inhibitory neurons within
451 each subject in Figure 3C despite the overall variability in selectivity across subjects).

452 Second, analyzing neural activity in the context of decision-making naturally led us to make
453 different comparisons than those carried out in previous work. For example, we measured
454 selectivity for a binary choice, while sensory tuning curves are measured in response to
455 continuously varying stimuli (e.g., orientation). Further, we measured activity in response to an
456 abstract stimulus, the meaning of which was learned gradually by the animal. This may recruit
457 circuits that differ from those supporting sensory processing in passively viewing mice. Finally,
458 we used stochastically fluctuating multisensory stimuli, which have not been evaluated in mouse
459 V1. Future studies that examine the tuning of V1 neurons to the sensory stimulus used here will
460 determine if V1 inhibitory neurons will be as sharply tuned as excitatory neurons to the stimulus.
461 This is a possibility: the tuning strength of interneurons can vary substantially for different
462 stimulus features. For instance, PV neurons in V1 have particularly poor tuning to the orientation
463 of visual stimuli, while their temporal-frequency tuning is considerably stronger (Znamenskiy et
464 al., 2018).

465 Our study addressed non only performance of well-trained animals, but also how acquiring
466 expertise modulates the activity of excitatory and inhibitory neurons in PPC. We observed that
467 learning induces an increase in the number of choice-selective neurons and a decrease in noise
468 correlations, indicating plasticity and reorganization of connections. As a result, population
469 responses preceding the two choices became progressively more distinct with training.
470 Importantly, these changes occur in parallel in both excitatory and inhibitory cells. Our findings
471 are partially in agreement with those in V1, in which learning improves tuning to sensory stimuli
472 in excitatory (Schoups et al., 2001; Poort et al., 2015; Khan et al., 2018) and some inhibitory
473 (Khan et al., 2018) subtypes. However, in V1 excitatory neurons have stronger tuning to sensory
474 stimuli early in training (Khan et al., 2018); in contrast, in our study the magnitude of choice
475 selectivity in PPC was the same for both cell types throughout training (Figure 8). Primate
476 studies have likewise observed that perceptual learning changes the selectivity of neurons
477 (Freedman and Assad, 2006; Law and Gold, 2008; Viswanathan and Nieder, 2015) and reduces
478 noise correlations (Gu et al., 2011; Ni et al., 2018).

479 Finally, we demonstrated that the learning-induced changes in PPC selectivity were closely
480 associated with the changes in animal performance, in keeping with primate studies of decision-
481 making (Law and Gold, 2008). This, together with our finding that changes in population activity
482 do not purely reflect movements (Figure S12), further corroborates the suggested role for PPC in
483 mapping sensation to action (Law and Gold, 2008; Raposo et al., 2014; Pho et al., 2018). Future
484 experiments using causal manipulations will reveal whether the increased choice selectivity we
485 observed in PPC originates there or is inherited from elsewhere in the brain.

486 By measuring cell-type-specific activity in parietal cortex during decision-making, we have
487 provided evidence that excitatory and inhibitory populations are equally choice-selective, and
488 that these ensembles emerge in parallel, as mice become skilled decision-makers. These results
489 argue against models with non-specific connectivity between excitatory and inhibitory neurons,
490 at least in decision circuits. In future modeling efforts, these features can be incorporated into
491 decision-making models, and their impact on key model outputs, such as reaction time
492 distributions and firing rates, can be evaluated. Such studies will shed light on how microcircuits
493 of inhibitory and excitatory neurons may vary across areas in their selectivity and specificity of
494 connections, and will reveal the circuit architectures that allow for equally selective inhibitory
495 and excitatory neurons.

496

497 **Methods**

498 **Imaging and behavioral dataset**

499 Our simultaneous imaging and decision-making dataset includes 135 sessions from 4 mice (45,
500 48, 7, and 35 sessions per mouse). Median number of trials per session is 213, 253, 264, and 222,
501 for each mouse. On average, 480 neurons were imaged per session, out of which ~40 neurons
502 were inhibitory and ~330 were excitatory. Approximately 100 neurons per session were not
503 classified as either excitatory or inhibitory since they did not meet our strict cell-type
504 classification criteria (see below). In 3 of the mice, the same group of neurons was imaged
505 throughout learning (35-48 training days).

506 **Mice and surgical procedure**

507 Gad2-IRES-CRE (Taniguchi et al., 2011) mice were crossed with Rosa-CAG-LSL-tdTomato-
508 WPRE (aka Ai14; Madisen et al., 2010) to create mice in which all GABAergic inhibitory
509 neurons were labeled. Adult mice (~2-month old) were used in the experiments. Meloxicam
510 (analgesic), dexamethasone (anti-inflammatory) and Baytril (enrofloxacin; anti-biotic) were
511 injected 30min before surgery. Using a biopsy punch, a circular craniotomy (diameter: 3mm)
512 was made over the left PPC (stereotaxic coordinates: 2 mm posterior, 1.7 mm lateral of bregma
513 (Harvey et al., 2012) under isoflurane (~5%) anesthesia. Pipettes (10-20 μ m in diameter, cut at
514 an angle to provide a beveled tip) were front-filled with AAV9-Synapsin-GCaMP6f (U Penn,
515 Vector Core Facility) diluted 2X in PBS (Phosphate-buffered saline). The pipette was slowly
516 advanced into the brain (Narishige MO-8 hydraulic micro-manipulator) to make ~3 injections of
517 50nL, slowly over an interval of ~5-10 min, by applying air pressure using a syringe. Injections
518 were made near the center of craniotomy at a depth of 250-350 μ m below the dura. A glass plug
519 consisting of a 5mm coverslip attached to a 3mm coverslip (using IR-curable optical bond,
520 Norland) was used to cover the craniotomy window. Vetbond, followed by metabond, was used
521 to seal the window. All surgical and behavioral procedures conformed to the guidelines
522 established by the National Institutes of Health and were approved by the Institutional Animal
523 Care and Use Committee of Cold Spring Harbor Laboratory.

524 **Imaging**

525 We used a 2-photon Moveable Objective Microscope with resonant scanning at approximately
526 30 frames per second (Sutter Instruments, San Francisco, CA). A 16X, 0.8 NA Nikon objective
527 lens was used to focus light on fields of view of size 512x512 pixels (~575 μ m x ~575 μ m). A
528 Ti:sapphire laser (Coherent) delivered excitation light at 930nm (average power: 20-70 mW).
529 Red (ET670/50m) and green (ET 525/50m) filters (Chroma Technologies) were used to collect
530 red and green emission light. The microscope was controlled by Mscan (Sutter). In mice in
531 which chronic imaging was performed during learning, the same plane was identified on
532 consecutive days using both coarse alignment, based on superficial blood vessels, as well as fine
533 alignment, using reference images of the red channel (tdTomato expression channel) at multiple
534 magnification levels. For each trial, imaging was started 500ms before the trial-initiation tone,
535 and continued 500ms after reward or time-out. We aimed to image in the center of the window
536 for all mice, but in one animal (Mouse 4), some tissue regrowth obscured the signal in this region
537 and so imaging was performed slightly further back.

538 **Decision-making behavior**

539 Mice were gradually water restricted over the course of a week, and were weighed daily. Mice
540 harvested at least 1 mL of water per behavioral/imaging session, and completed 100-500 trials
541 per session. After approximately one week of habituation to the behavioral setup, 15-30 training
542 days were required to achieve 75% correct choice. Animal training took place in a sound
543 isolation chamber. The stimulus in all trials was multisensory, consisting of a series of
544 simultaneous auditory clicks and visual flashes, occurring with Poisson statistics (Brunton et al.,
545 2013; Odoemene et al., 2017). Multisensory stimuli were selected because they increased the
546 learning rate of the mice, a critical consideration since GCaMP6f expression can be unreliable
547 over a long period of time. Stimulus duration was 1000 ms. Each pulse was 5 ms; minimum
548 interval between pulses was 32 ms, and maximum interval was 250 ms. The pulse rate ranged
549 from 5 to 27 Hz. The category boundary for marking high-rate and low-rate stimuli was 16 Hz,
550 at which animals were rewarded randomly on either side. The highest stimulus rates used here
551 are known to elicit reliable, steady state flicker responses in retinal ERG in mice (Krishna et al.,
552 2002; Tanimoto et al., 2015).

553 Mice were on top of a cylindrical wheel and a rotary encoder was used to measure their running
554 speed. Trials started with a 50 ms initiation tone (Figure S1A). Mice had 5 sec to initiate a trial
555 by licking the center waterspout (Marbach and Zador, 2017), after which the multisensory
556 stimulus was played for 1 second. If mice again licked the center waterspout, they received 0.5
557 μL water on the center spout, and a 50ms go cue was immediately played. Animals had to report
558 a choice by licking to the left or right waterspout within 2 sec. Mice were required to confirm
559 their choice by licking the same waterspout one more time within 300 ms after the initial lick
560 (Marbach and Zador, 2017). The “confirmation lick” helped dissociate the choice time (i.e. the
561 time of first lick to the side waterspout), from the reward time (i.e. the time of second lick to the
562 side waterspout); it also helped with reducing impulsive choices. If the choice was correct, mice
563 received 2-4 μL water on the corresponding waterspout. An incorrect choice was punished with a
564 2 sec time-out. The experimenter-imposed inter-trial intervals (ITIs) were drawn from a
565 truncated exponential distribution, with minimum, maximum, and lambda equal to 1 sec, 5 sec,
566 and 0.3 sec, respectively. However, the actual ITIs could be much longer depending on when the
567 animal initiates the next trial. Bcontrol (Raposo et al., 2014) with a Matlab interface was used to
568 deliver trial events (stimulus, reward, etc) and collect data.

569 **Logistic regression model of behavior**

570 A modified version of a logistic regression model in (Busse et al., 2011) was used to assess the
571 extent to which the animal’s choice depends on the strength of sensory evidence (how far the
572 stimulus rate is from the category boundary at 16Hz), the previous choice outcome (success or
573 failure) and ITI, (the time interval between the previous choice and the current stimulus onset)
574 (Figure S1B). The model has the form

$$575 \quad p = \frac{1}{1+e^{-z}} \quad \text{eq. 1}$$

$$576 \quad z = \beta_0 + (\beta_{r1} R_1 + \beta_{r2} R_2 + \beta_{r3} R_3 + \beta_{r4} R_4 + \beta_{r5} R_5 + \beta_{r6} R_6) + (\beta_{s1} S_1 + \beta_{s2} S_2) + (\beta_{f1} F_1 + \beta_{f2} F_2)$$

577 where p is the probability of choosing left. Stimulus strength (R) was divided into 6 bins (R_1 to

578 R_6). Previous success (S) was divided into 2 bins (S_1 to S_2), with S_1 referring to success after a
579 long ITI (> 7 sec) and S_2 to success after a short ITI (< 7 sec). Previous failure (F) was divided
580 into 2 bins (F_1 to F_2), with F_1 referring to failure after a long ITI and F_2 to failure after a short
581 ITI. For example, if a trial had stimulus strength 3 Hz, and was preceded by a success choice
582 with ITI 5 sec, then R_2 and S_1 would be set to 1 and all other R, S and F parameters to 0 (Figure
583 S1B).

584 For each session the scalar coefficients β_0 , β_{r1} to β_{r6} , β_{s1} , β_{s2} , β_{f1} , and β_{f2} were fit using Matlab
585 `glmfit.m`. Figure S1B left shows β_{r1} to β_{r6} . Figure S1B middle shows β_{s1} and β_{s2} , and Figure S1B
586 right shows β_{f1} and β_{f2} .

587 **ROI (region of interest) extraction and deconvolution**

588 The recorded movies from all trials were concatenated and corrected for motion artifacts by
589 cross-correlation using Discrete Fourier Transform (DFT) registration (Guizar-Sicairos et al.,
590 2008). Subsequently, active ROIs (sources) were extracted using the Constrained Nonnegative
591 Matrix Factorization (CNMF) algorithm (Pnevmatikakis et al., 2016) as implemented in the
592 CaImAn package (Giovannucci et al., 2019) in MATLAB. The traces of the identified neurons
593 were $\Delta F/F$ normalized and then deconvolved by adapting the FOOPSI deconvolution algorithm
594 (Vogelstein et al., 2010; Pnevmatikakis et al., 2016) to a multi-trial setup. This was necessary
595 because simply concatenating individual trials would lead to discontinuities in the traces, which
596 could distort estimates of the time constants. Each value of Foopsi deconvolution represents
597 spiking activity at each frame for a given neuron. We have referred to the deconvolved values as
598 "inferred spiking activity" throughout the paper. The deconvolved values do not represent
599 absolute firing rates, so they cannot be compared across neurons. However, for a particular
600 neuron, higher inferred spiking activity means higher firing rate. We elected to base our analyses
601 on inferred spiking activity rather than fluorescence activity because peak amplitudes and time
602 constants of the fluorescence responses vary across neurons, affecting subsequent analyses
603 (Machado et al., 2015; Helmchen and Tank, 2019).

604 We adapted the FOOPSI for multi-trial setup as follows. For each component, the activity trace
605 over all the trials was used to determine the time constants of the calcium indicator dynamics as
606 in (Pnevmatikakis et al., 2016). Then the neural activity during each trial was deconvolved
607 separately using the estimated time constant and a zero baseline (since the traces were $\Delta F/F$
608 normalized). A difference of exponentials was used to simulate the rise and decay of the
609 indicator.

610 **Neuropil Contamination removal**

611 The CNMF algorithm demixes the activity of overlapping neurons. It takes into account
612 background neuropil activity by modeling it as a low rank spatiotemporal matrix (Pnevmatikakis
613 et al., 2016). In this study a rank two matrix was used to capture the neuropil activity. To
614 evaluate its efficacy, we compared the traces obtained from CNMF to the traces from a "manual"
615 method similar to (Chen et al., 2013) (Figure S14): the set of spatial footprints (shapes) extracted
616 from CNMF were binarized by thresholding each component at 20% of its maximum. The binary
617 masks were then used to average the raw data and obtain an activity trace that also included
618 neuropil effects. To estimate the background signal, an annulus around the binary mask was

619 constructed with minimum distance 3 pixels from the binary mask and width 7 pixels (Figure
 620 S14A). The average of the raw data over the annulus defined the background trace, which was
 621 subtracted from the activity trace. The resulting trace was then compared with the CNMF
 622 estimated temporal trace for this activity. The comparison showed a very high degree of
 623 similarity between the two traces (Figure S14; example component; $r=0.96$), with the differences
 624 between the components being attributed to noise and not neuropil related events. Note that this
 625 “manual” approach is only applicable in the case when the annulus does not overlap with any
 626 other detected sources. These results demonstrate the ability of the CNMF framework to properly
 627 capture neuropil contamination and remove it from the calcium traces.

628 **ROI inclusion criteria**

629 We excluded poor-quality ROIs identified by the CNMF algorithm based on a combination of
 630 criteria: 1) size of the spatial component, 2) decay time constant, 3) correlation of the spatial
 631 component with the raw ROI image built by averaging spiking frames, 4) correlation of the
 632 temporal component with the raw activity trace, and 5) the probability of fluorescence traces
 633 maintaining values above an estimated signal-to-noise level for the expected duration of a
 634 calcium transient (Giovannucci et al., 2018) (GCaMP6f, frame rate: 30Hz). A final manual
 635 inspection was performed on the selected ROIs to validate their shape and trace quality.

636 **Identification of inhibitory neurons**

637 We used a two-step method to identify inhibitory neurons. First, we corrected for bleed-through
 638 from green to red channel by considering the following regression model,

$$639 \mathbf{r}_i(t) = \beta_i \mathbf{1}_p + s \mathbf{g}_i(t) + \epsilon \quad eq. 2.$$

640 where, $\mathbf{r}_i(t)$ and $\mathbf{g}_i(t)$ are vectors, indicating pixel intensity in red and green channel,
 641 respectively, with each component of the vector corresponding to one pixel in the ROI, i labels
 642 ROI (presumably each ROI is a neuron), β_i is the offset, $\mathbf{1}_p$ is a vector whose components are all
 643 1, and s is the parameter that tells us how much of the green channel bleeds through to the red
 644 one..

645 It is the parameter s that we are interested in. To find s , we define a cost function, C ,

$$646 C = \int dt \sum_i |\mathbf{r}_i(t) - \beta_i \mathbf{1}_p + s \mathbf{g}_i(t)|^2 \quad eq. 3$$

647 and minimize it with respect to s and all the β_i . The value of s at the minimum reflects the
 648 fraction of bleed-through from the green to the red channel. That value, denoted s^* , is then used
 649 to compute the bleedthrough-corrected image of the red-channel, denoted I via the expression

$$650 I = R - s^* G \quad eq. 4$$

651 where R and G are the time-averaged images of the red and green channels, respectively.

652 Once the bleedthrough-corrected image, I , was computed, we used it to identify inhibitory
 653 neurons using two measures,

654 1) A measure of local contrast, by computing, on the red channel (I , eq. 4), the average pixel
 655 intensity inside each ROI mask relative to its immediate surrounding mask (width=3 pixels).

656 Given the distribution of contrast levels, we used two threshold levels, T_E and T_I , defined,
657 respectively, as the 80th and 90th percentiles of the local contrast measures of all ROIs. ROIs
658 whose contrast measure fell above T_I were identified as inhibitory neurons. ROIs whose contrast
659 measure fell below T_E were identified as excitatory neurons, and ROIs with the contrast measure
660 in between T_E and T_I were not classified as either group (“unsure” class).

661 2) In addition to a measure of local contrast, we computed for each ROI the correlation between
662 the spatial component (ROI image on the green channel) and the corresponding area on the red
663 channel. High correlation values indicate that the ROI on the green channel has a high signal on
664 the red channel too; hence the ROI is an inhibitory neuron. We used this correlation measure to
665 further refine the neuron classes computed from the local contrast measure (i.e. measure 1
666 above). ROIs that were identified as inhibitory based on their local contrast (measure 1) but had
667 low red-green channel correlation (measure 2), were reset as “unsure” neurons. Similarly, ROIs
668 that were classified as excitatory (based on their local contrast) but had high red-green channel
669 correlation were reclassified as unsure. Unsure ROIs were included in the analysis of all-neuron
670 populations (Figure 3A left); but were excluded from the analysis of excitatory only or inhibitory
671 only populations (Figure 3A middle, right). Finally, we manually inspected the ROIs identified
672 as inhibitory to confirm their validity. [This method resulted in 11% inhibitory neurons, which is](#)
673 [within the range of previous studies \(10-20%: Rudy et al., 2011\); \(15%: Beaulieu, 1993\); \(16%:](#)
674 [Gabbott et al., 1997\); \(<5%: de Lima and Voigt, 1997\); \(10-25%: de Lima et al., 2009\).](#)

675 **General analysis procedures**

676 All analyses were performed on inferred spiking activity. Traces were down-sampled, so each
677 bin was the non-overlapping moving average of 3 frames (97.1 ms, which we refer to as 97 ms).
678 Inferred spiking activity for each neuron was normalized so the max spiking activity for each
679 neuron equaled 1. The trace of each trial was aligned to the time of the choice (i.e. the time of the
680 1st lick to either of the side waterspouts after the go tone). Two-tailed t-test was performed for
681 testing statistical significance. Summary figures including all mice were performed on the time
682 bin preceding the choice, i.e. 0-97 ms before choice onset. All reported correlations are Pearson’s
683 coefficients. Analyses were performed in Python and Matlab.

684 **ROC analysis**

685 The area under the ROC curve (AUC) was used to measure the choice preference of single
686 neurons. Choice selectivity was defined as the absolute deviation of AUC from chance level:
687 choice selectivity = $2*|AUC-0.5|$. To identify significantly choice-selective neurons, for each
688 neuron we performed ROC on shuffled trial labels (i.e. left and right choices were randomly
689 assigned to each trial). This procedure was repeated 50 times to create a distribution of shuffled
690 AUC values for each neuron (Figure S3A, “shuffled”). A neuron’s choice selectivity was
691 considered to be significant if the probability of the actual AUC (Figure S3A, “real”) being
692 drawn from the shuffled AUC distribution was less than 0.05. Time points from 0–97 ms before
693 the decision were used to compute the fraction of choice-selective neurons (Figure 2B; Figure
694 8G).

695 **Decoding population activity**

696 A linear SVM (Python sklearn package) was trained on each bin of the population activity in
697 each session (non-overlapping 97ms time bins). To break any dependencies on the sequence of
698 trials, we shuffled the order of trials for the entire population. To avoid bias in favor of one
699 choice over the other, we matched the number of left- and right-choice trials used for classifier
700 training. L2 regularization was used to avoid over-fitting. 10-fold cross validation was performed
701 by leaving out a random 10% subset of trials to test the classifier performance, and using the
702 remaining trials for training the classifier. This procedure was repeated 50 times. A range of
703 regularization values was tested, and the one that gave the smallest error on the validation dataset
704 was chosen as the optimal regularization parameter. Classifier accuracy was computed as the
705 percentage of testing trials in which the animal's choice was accurately predicted by the
706 classifier, and summarized as the average across the 50 repetitions of trial subsampling. A
707 minimum of 10 correct trials per choice was required in order to run the SVM on a session.
708 Inferred spiking activity of each neuron was z-scored before running the SVM.

709 When comparing classification accuracy for excitatory vs. inhibitory neurons, the excitatory
710 population was randomly sub-sampled to match the population size of inhibitory neurons to
711 enable a fair comparison (Figure 3, blue vs. red). To compare the distribution of weights in the
712 all-neuron classifier (Figure 3 black), the weight vector for each session was normalized to unity
713 length (Figure 3D-F).

714 When decoding the stimulus category (Figure S6B), we used stimulus-aligned trials, and avoided
715 any contamination by the choice signal by sub-selecting equal number of left and right choice
716 trials for each stimulus category. When decoding trial outcome (Figure S6C), we used outcome-
717 aligned trials, and avoided contamination by the choice or stimulus signal by subselecting equal
718 number of trials from left and right choice trials for each trial outcome.

719 **Stability**

720 To test the stability of the population code, decoders were trained and tested at different time
721 bins (Kimmel et al., 2016) (Figure 4). To avoid the potential effects of auto-correlation, we
722 performed cross validation not only across time bins, but also across trials. In other words, even
723 though the procedure was cross validated by testing the classifier at a time different from the
724 training time, we added another level of cross-validation by testing on a subset of trials that were
725 not used for training. This strict method allowed our measure of stability duration to be free of
726 auto-correlation effects.

727 As an alternative measure of stability, the angle between pairs of classifiers that were trained at
728 different moments in the trial was computed (Figure S10C). Small angles indicate alignment,
729 hence stability, of the classifiers. Large angles indicate misalignment, i.e. instability of the
730 classifiers.

731 **Noise correlations**

732 To estimate noise correlations, the order of trials was shuffled for each neuron independently.
733 Shuffling was done within the trials of each choice, hence retaining the choice signal, while de-
734 correlating the population activity to remove noise correlations. Then we classified population
735 activity in advance of left vs. right choice (at time bin 0–97 ms before the choice) using the de-
736 correlated population activity. This procedure was performed on neural ensembles of

737 increasingly larger size, with the most selective neurons (the ones with the largest value of
738 $|AUC-0.5|$) added first (Figure 7A). To summarize how noise correlations affected classification
739 accuracy in the population (Figure 7B), we computed, for the largest neural ensemble (Figure
740 7A, max value on the horizontal axis), the change in classifier accuracy in the de-correlated data
741 (“pseudo populations”) vs. the original data. This analysis was only performed for the entire
742 population; the small number of inhibitory neurons in each session prevented a meaningful
743 comparison of classification accuracy on real vs. pseudo populations.

744 To measure pairwise noise correlations, we subtracted the trial-averaged response to a particular
745 choice from the response of single trials of that choice. This allowed removing the effect of
746 choice on neural responses. The remaining variability in trial-by-trial responses can be attributed
747 to noise correlations, measured as the Pearson correlation coefficient for neuron pairs. We also
748 measured noise correlations using the spontaneous activity defined as the neural responses in 0-
749 97 ms preceding the trial initiation tone (Figure S10A,C). We computed the pairwise correlation
750 coefficient (Pearson) for a given neuron with each other neuron within an ensemble (e.g.,
751 excitatory neurons). The resulting coefficients were then averaged to generate a single
752 correlation value for that neuron. This was repeated for all neurons within the ensemble (Figure
753 6).

754 To compute pairwise correlations on excitatory and inhibitory neurons with the same inferred
755 spiking activity (Figure S10D,E), we computed the median inferred spiking activity across trials
756 for individual excitatory and inhibitory neurons in a session. The medians were then divided into
757 50 bins. The firing-rate bin that included the maximum number of inhibitory neurons was
758 identified (“max bin”); inhibitory and excitatory neurons whose firing rate was within this “max
759 bin” were used for the analysis. The firing rates were matched for these neurons because their
760 median firing rate was within the same small bin of firing rates. Pairwise correlations were then
761 computed as above.

762 **Learning analysis**

763 In 3 of the mice, the same field of view was imaged each session during learning. This was
764 achieved in two ways. First, the vasculature allowed a coarse alignment of the imaging location
765 from day to day. Second, the image from the red channel was used for a finer alignment. Overall,
766 most neurons were stably present across sessions (Figure S11). This suggests that we likely
767 measured activity from a very similar population each day. Importantly, however, our
768 conclusions do not rely on this assumption: our measures and findings focus on learning-related
769 changes in the PPC population overall, as opposed to tracking changes in single neurons. To
770 assess how population activity changed over learning, we evaluated classification accuracy each
771 day, training a new decoder for each session. This approach allowed us to compute the best
772 decoding accuracy for each session.

773 “Early days” (Figure 8; Figures S12,S13) included the initial training days in which the animal’s
774 performance, defined as the fraction of correct choices on easy trials, was lower than the 20th
775 percentile of performance across all days. “Late days” (Figure 8; Figures S12,S13) included the
776 last training days in which the animal’s behavioral performance was above the 80th percentile of
777 performance across all days.

778 To measure the timing of decision-related activity (Figure 8C,E), we identified all sessions in
 779 which classifier accuracy was significantly different than the shuffle (t-test, $p < 0.05$) over a
 780 window of significance that was at least 500 ms long. We defined the “choice signal onset”
 781 (Figure 8C,E) as the trial time corresponding to the first moment of that window. Sessions in
 782 which the 500 ms window of significance was present are included in Figure 8C. The number of
 783 points (and hence the relationship between session number and color in Figure 8C) differs
 784 slightly across the three groups. This is because on some sessions, the window of significance
 785 was present in one group but not another. For example, in a session the population including all
 786 neurons might have a 500 ms window of significance, hence it will contribute a point to Figure
 787 7C left, while the population with only inhibitory neurons might be only transiently significant
 788 for < 500 ms, hence it will be absent from Figure 8C right.

789 Modeling decision circuits

790 We considered a linearized rate network of the form

$$791 \quad \begin{aligned} \frac{d\mathbf{v}_E}{dt} &= -\mathbf{v}_E + \mathbf{W}_{EE} \cdot \mathbf{v}_E - \mathbf{W}_{EI} \cdot \mathbf{v}_I + \mathbf{h}_s + \boldsymbol{\xi}_E \\ \frac{d\mathbf{v}_I}{dt} &= -\mathbf{v}_I + \mathbf{W}_{IE} \cdot \mathbf{v}_E - \mathbf{W}_{II} \cdot \mathbf{v}_I + \boldsymbol{\xi}_I \end{aligned}$$

792 where E and I refer to the excitatory and inhibitory populations, respectively, \mathbf{v}_E and \mathbf{v}_I are
 793 vectors of firing rates ($\mathbf{v}_E = v_{E1}, v_{E2}, \dots$, and similarly for \mathbf{v}_I), \mathbf{W}_{EE} , \mathbf{W}_{EI} , \mathbf{W}_{IE} and \mathbf{W}_{II} are the
 794 connectivity matrices (\mathbf{W}_{EI} indicates connection from inhibitory to excitatory neuron), \mathbf{h}_s is the
 795 input, with s either 1 or 2 (corresponding to left and right licks), and $\boldsymbol{\xi}$ is trial to trial noise, taken
 796 to be zero mean and Gaussian, with covariance matrices

$$797 \quad \begin{aligned} \langle \boldsymbol{\xi}_E \boldsymbol{\xi}_E \rangle &= \boldsymbol{\Sigma}_{EE} \\ \langle \boldsymbol{\xi}_I \boldsymbol{\xi}_I \rangle &= \boldsymbol{\Sigma}_{II}. \end{aligned}$$

798

799 For the input we’ll assume that about half the elements of \mathbf{h}_s are h_0 for the rightward choice and
 800 $-h_0$ for the leftward choice, and the rest are $-h_0$ for the rightward choice and h_0 for the leftward
 801 choice. We used $h_0 = 0.1$ (see Table 1). The noise covariance is diagonal but non-identity, with
 802 diagonal elements distributed as

$$803 \quad \begin{aligned} \sqrt{\Sigma_{EE,ii}} &\sim \text{Unif}\left(\sigma - \frac{\delta}{2}, \sigma + \frac{\delta}{2}\right) \\ \sqrt{\Sigma_{II,ii}} &\sim \text{Unif}\left(\sigma - \frac{\delta}{2}, \sigma + \frac{\delta}{2}\right). \end{aligned}$$

804

805 The goal is to determine the value of s (that is, determine whether \mathbf{h}_1 or \mathbf{h}_2 was present) given
 806 the activity of a subset of the neurons from either the excitatory or inhibitory populations. We’ll
 807 work in steady state, for which

808
$$\mathbf{v}_E = \mathbf{W}_{EE} \cdot \mathbf{v}_E - \mathbf{W}_{EI} \cdot \mathbf{v}_I + \mathbf{h}_s + \boldsymbol{\xi}_E$$

809
$$\mathbf{v}_I = \mathbf{W}_{IE} \cdot \mathbf{v}_E - \mathbf{W}_{II} \cdot \mathbf{v}_I + \boldsymbol{\xi}_I.$$

809 Solving for \mathbf{v}_E and \mathbf{v}_I yields

810
$$\mathbf{v}_E = \mathbf{J}_E \cdot (\mathbf{h}_s + \boldsymbol{\xi}_E - \tilde{\mathbf{W}}_{EI} \cdot \boldsymbol{\xi}_I)$$

810
$$\mathbf{v}_I = \mathbf{J}_I \cdot (\boldsymbol{\xi}_I + \tilde{\mathbf{W}}_{IE}(\mathbf{h}_s + \boldsymbol{\xi}_E))$$

811 where

812
$$\mathbf{J}_E \equiv (\mathbf{I} - \mathbf{W}_{EE} + \tilde{\mathbf{W}}_{EI} \cdot \mathbf{W}_{IE})^{-1}$$

812
$$\mathbf{J}_I \equiv (\mathbf{I} + \mathbf{W}_{II} + \tilde{\mathbf{W}}_{IE} \cdot \mathbf{W}_{EI})^{-1}$$

812
$$\tilde{\mathbf{W}}_{EI} \equiv \mathbf{W}_{EI}(\mathbf{I} + \mathbf{W}_{II})^{-1}$$

812
$$\tilde{\mathbf{W}}_{IE} \equiv \mathbf{W}_{IE}(\mathbf{I} - \mathbf{W}_{EE})^{-1},$$

813 and \mathbf{I} is the identity matrix. We are interested in the decoding accuracy of a sub-population of
 814 neurons. For that we'll use a matrix \mathbf{D}_n that picks out n components of whatever it's operating
 815 on. So, for instance, $\mathbf{D}_n \cdot \mathbf{v}_E$ is an n -dimensional vector with components equal to n of the
 816 components of \mathbf{v}_E .

817 For a linear and Gaussian model such as ours, in which the covariance is independent of s , we
 818 need two quantities to compute the performance of an optimal decoder: the difference in the
 819 means of the subsampled populations when \mathbf{h}_1 versus \mathbf{h}_2 are present, and covariance matrix of
 820 the subsampled populations. The difference in means are given by

821
$$\Delta\langle \mathbf{D}_n \cdot \mathbf{v}_E \rangle = \mathbf{D}_n \cdot \mathbf{J}_E \cdot \Delta \mathbf{h}$$

821
$$\Delta\langle \mathbf{D}_n \cdot \mathbf{v}_I \rangle = \mathbf{D}_n \cdot \mathbf{J}_I \cdot \tilde{\mathbf{W}}_{IE} \cdot \Delta \mathbf{h}$$

822 where $\Delta \mathbf{h}$ is the difference between the two inputs,

823
$$\Delta \mathbf{h} \equiv \mathbf{h}_1 - \mathbf{h}_2.$$

824 The covariances are given by

825
$$\text{Cov}[\mathbf{D}_n \cdot \mathbf{v}_E] = \mathbf{D}_n \cdot \mathbf{J}_E \cdot [\boldsymbol{\Sigma}_{EE} + \tilde{\mathbf{W}}_{EI} \cdot \boldsymbol{\Sigma}_{II} \cdot \tilde{\mathbf{W}}_{EI}^T] \cdot \mathbf{J}_E^T \cdot \mathbf{D}_n^T$$

825
$$\text{Cov}[\mathbf{D}_n \cdot \mathbf{v}_I] = \mathbf{D}_n \cdot \mathbf{J}_I \cdot [\boldsymbol{\Sigma}_{II} + \tilde{\mathbf{W}}_{IE} \cdot \boldsymbol{\Sigma}_{EE} \cdot \tilde{\mathbf{W}}_{IE}^T] \cdot \mathbf{J}_I^T \cdot \mathbf{D}_n^T$$

826 where T denotes transpose. Combining the mean and covariance gives us the signal to noise
 827 ratio,

828
$$(S/N)_E = \Delta \mathbf{h} \cdot \mathbf{J}_E^T \cdot \mathbf{D}_n^T \cdot (\mathbf{D}_n \cdot \mathbf{J}_E \cdot [\boldsymbol{\Sigma}_{EE} + \tilde{\mathbf{W}}_{EI} \cdot \boldsymbol{\Sigma}_{II} \cdot \tilde{\mathbf{W}}_{EI}^T] \cdot \mathbf{J}_E^T \cdot \mathbf{D}_n^T)^{-1} \cdot \mathbf{D}_n \cdot \mathbf{J}_E \cdot \Delta \mathbf{h}$$

828
$$(S/N)_I = \Delta \mathbf{h} \cdot \tilde{\mathbf{W}}_{IE}^T \cdot \mathbf{J}_I^T \cdot \mathbf{D}_n^T \cdot (\mathbf{D}_n \cdot \mathbf{J}_I \cdot [\boldsymbol{\Sigma}_{II} + \tilde{\mathbf{W}}_{IE} \cdot \boldsymbol{\Sigma}_{EE} \cdot \tilde{\mathbf{W}}_{IE}^T] \cdot \mathbf{J}_I^T \cdot \mathbf{D}_n^T)^{-1} \cdot \mathbf{D}_n \cdot \mathbf{J}_I \cdot \tilde{\mathbf{W}}_{IE} \cdot \Delta \mathbf{h}.$$

829 The performance of an optimal decoder is then given by

830
$$\text{fraction correct} = \Phi\left(\frac{\sqrt{S/N}}{\sqrt{2}}\right)$$

831 where Φ is the cumulative normal function. All of our analysis is based on this expression.
 832 Differences in fraction correct depend only on differences in the connectivity matrices, which we
 833 describe next.

834 Connectivity matrices

835 We consider three connectivity structures: completely non-selective, signal-selective, and signal-
 836 to-noise selective (corresponding to Figures 5A, 5B and 5C, respectively). In all cases the
 837 connectivity is sparse (the connection probability between any two neurons is 0.1). What differs
 838 is the connection strength when neurons are connected. We describe below how the connection
 839 strength is chosen for our three connectivity structures.

840 *Non-selective.* The connectivity matrices have the especially simple form

$$841 \quad \mathbf{W}_{\alpha\beta,ij} = \begin{cases} \frac{w_{\alpha\beta}}{\sqrt{cN}} & \text{with probability } c \\ 0 & \text{otherwise} \end{cases}$$

842 where $\alpha, \beta \in \{E, I\}$, $N (\equiv N_E + N_I)$ is the total number of neurons, and $w_{\alpha\beta}$ are parameters (see
 843 Table 1).

844 *Signal-selective.* We divide the neurons into two sets of excitatory and inhibitory sub-
 845 populations, as in Figure 5B. The connection strengths are still given by the above expression,
 846 but now α and β acquire subscripts that specify which population they are in: $\alpha, \beta \in$
 847 $\{E_1, E_2, I_1, I_2\}$, with E_1 and I_1 referring to population 1 and E_2 and I_2 to population 2. The
 848 within-population connection strengths are the same as for the non-selective population ($w_{\alpha_i\beta_i} =$
 849 $w_{\alpha\beta}, i = 1, 2$), but the across-population connection strengths are smaller by a factor of ρ ,

$$850 \quad \frac{w_{\alpha_i\beta_j}}{w_{\alpha_i\beta_i}} = \rho$$

851 for $i = 1$ and $j = 2$ or vice-versa. The value of ρ determines how selective the sub-populations
 852 are: $\rho = 0$ corresponds to completely selective sub-populations while $\rho = 1$ corresponds to the
 853 completely non-selective case.

854 *SNR- selective.* We choose the connectivity as in the non-selective case, and then change
 855 synaptic strength so that the inhibitory neurons receive stronger connections from the excitatory
 856 neurons with high signal to noise ratios. To do that, we first rank excitatory units in order of
 857 ascending signal to noise ratio (by using \mathbf{D}_1 in the expression for $(S/N)_E$ in the previous
 858 section). We then make the substitution

$$859 \quad W_{IE,ij} \rightarrow W_{IE,ij} \left(\frac{r_j}{N_E} \right)^4$$

860 where r_j is the rank of excitatory j in the order of ascending signal to noise ratio and, recall, N_E
 861 is the number of excitatory neurons. This downweights projections from low signal to noise ratio
 862 excitatory neurons and upweights connections from high signal to noise ratio neurons. Finally,
 863 all elements are scaled to ensure that the average connection strength from the excitatory to the
 864 inhibitory network is the same as before the substitution.

865 Simulation details

866 The simulation parameters are given in Table 1. In addition, there are a number of relevant
 867 details, the most important of which is related to the input, \mathbf{h}_s . As mentioned in the previous
 868 section, about half the elements of \mathbf{h}_s are h_0 for the rightward choice and $-h_0$ for the leftward
 869 choice, and the rest are h_0 for the leftward choice $-h_0$ for the rightward choice. This is strictly
 870 true for the completely non-selective and signal to noise selective connectivity; for the signal
 871 selective connectivity, we use $\mathbf{h}_{s,i} = h_0$ for the rightward choice and $-h_0$ for the leftward
 872 choice when excitatory neuron i is in population 1, and $\mathbf{h}_{s,i} = h_0$ for the leftward choice and
 873 $-h_0$ for the rightward choice when excitatory neuron i is in population 2. In either case,
 874 however, this introduces a stochastic element: for the completely non-selective and signal to
 875 noise selective connectivities, there is randomness in both the input and the circuit; for the signal
 876 selective connectivity, there is randomness in the circuit. In the former case, we can eliminate the
 877 randomness in the connectivity by averaging over the input, as follows.

878 Because the components of $\Delta\mathbf{h}$ are independent, we have

$$879 \quad \langle \Delta h_{s,i} \Delta h_{s,j} \rangle = \delta_{ij} \langle \Delta h_{s,i}^2 \rangle$$

880 where δ_{ij} is the Kronecker delta ($\delta_{ij} = 1$ if $i = j$ and zero otherwise). Because $\Delta h_{s,i}$ is either
 881 $+h_0$ or $-h_0$, we have

$$882 \quad \langle \Delta \mathbf{h} \Delta \mathbf{h} \rangle = 4h_0^2 \mathbf{I}$$

883 where \mathbf{I} is the identity matrix. Thus, when we average the signal to noise ratios over $\Delta\mathbf{h}$, the
 884 expressions simplify slightly,

$$885 \quad \frac{\langle (S/N)_E \rangle}{4h_0^2} = \text{trace} \left\{ (\mathbf{D}_n \cdot \mathbf{J}_E \cdot [\boldsymbol{\Sigma}_{EE} + \tilde{\mathbf{W}}_{EI} \cdot \boldsymbol{\Sigma}_{II} \cdot \tilde{\mathbf{W}}_{EI}^T] \cdot \mathbf{J}_E^T \cdot \mathbf{D}_n^T)^{-1} \cdot \mathbf{D}_n \cdot \mathbf{J}_E \cdot \mathbf{J}_E^T \cdot \mathbf{D}_n^T \right\}$$

$$\frac{\langle (S/N)_I \rangle}{4h_0^2} = \text{trace} \left\{ (\mathbf{D}_n \cdot \mathbf{J}_I \cdot [\boldsymbol{\Sigma}_{II} + \tilde{\mathbf{W}}_{IE} \cdot \boldsymbol{\Sigma}_{EE} \cdot \tilde{\mathbf{W}}_{IE}^T] \cdot \mathbf{J}_I^T \cdot \mathbf{D}_n^T)^{-1} \cdot \mathbf{D}_n \cdot \mathbf{J}_I \cdot \tilde{\mathbf{W}}_{IE} \cdot \tilde{\mathbf{W}}_{IE}^T \cdot \mathbf{J}_I^T \cdot \mathbf{D}_n^T \right\}.$$

886 To avoid having to numerically average over input, we used these expressions when computing
 887 decoding accuracy for the completely non-selective and signal to noise selective connectivity.
 888 That left us with some randomness associated with the networks (as connectivity is chosen
 889 randomly), but that turned out to produce only small fluctuations, so each data point in Figures
 890 5A and 5C was from a single network. For the signal selective connectivity (Figure 5B), the
 891 network realization turned out to matter, so we averaged over 25 networks, and for each of them
 892 we did a further averaging over 100 random picks of the 50 neurons from which we decoded.

893 In Figure 5, the x-axis is the ratio of the average connection strength from excitatory to
 894 inhibitory neurons to the average connection strength from inhibitory to excitatory neurons. This
 895 was chosen because it turned out to be the connectivity parameter with the largest effect on
 896 decoding accuracy. That in turn is because it turns out to be equivalent to the input noise to the
 897 inhibitory population. To see why, make the substitution

$$898 \quad \begin{aligned} \mathbf{W}_{IE} &\rightarrow \gamma \mathbf{W}_{IE} \\ \mathbf{W}_{EI} &\rightarrow \gamma^{-1} \mathbf{W}_{EI}. \end{aligned}$$

899 By letting $\mathbf{v}_I \rightarrow \gamma \mathbf{v}_I$, we see that this is formally equivalent to letting $\xi_I \rightarrow \gamma^{-1} \xi_I$, which in turn
 900 corresponds to letting $\Sigma_{II} \rightarrow \gamma^{-2} \Sigma_{II}$. Thus the x-axis in Figure 5 can be thought of as the axis of
 901 decreasing input noise to the inhibitory neurons.

902 Table 1. Parameters used in simulations

σ	1.25	noise level
δ	0.75	breadth of noise level distribution
w_{EE}	0.25	excitatory \rightarrow excitatory coupling
w_{II}	-2	inhibitory \rightarrow inhibitory coupling
w_{IE}	0.87	excitatory \rightarrow inhibitory coupling
w_{EI}	-0.87	inhibitory \rightarrow excitatory coupling
c	0.1	connection probability
N_E	4000	number of excitatory neurons
N_I	1000	number of inhibitory neurons
n	50	number of readout neurons
h_0	0.1	input strength
ρ	0.75	selectivity index

903

904 **Data and code availability**

905 All the data used in the paper are publicly available on CSHL repository:
 906 <http://repository.cshl.edu/36980/>. Further, all the data is converted into the NWB format
 907 (Neurodata Without Borders (Teeters et al., 2015; Ruebel et al., 2019), and is available on
 908 CSHL repository: <https://dx.doi.org/10.14224/1.37693>

909 Code for data processing and analysis is publicly available on github:
 910 https://github.com/farznaj/imaging_decisionMaking_exc_inh

911 Code for converting data to NWB format is also available on github:
 912 <https://github.com/vathes/najafi-2018-nwb>

913 **Author Contributions**

914 Conceptualization and Writing: FN and AKC. Experiments and Analysis: FN. Decoding
915 methodology and common-slope regression model: GFE, JPC and FN. Circuit modeling: RC and
916 PEL. Spike-inference methodology: EAP. Funding Acquisition, Resources and Supervision:
917 AKC.

918 **Acknowledgements**

919 We thank Hien Nguyen for help with training mice, Matt Kaufman, Kachi Odoemene, Fred
920 Marbach for technical assistance and thoughtful conversations. We thank Andrea Giovannucci
921 for help with ROI inclusion criteria #5. We thank Ashley Juavinett, Simon Musall, and Sashank
922 Pisupati for helpful discussions and feedback on early versions of the manuscript. [We thank](#)
923 [Thinh Nguyen, Dimitri Yatsenko and Edgar Walker for help with data conversion into the NWB](#)
924 [format](#). The work was supported by the Simons Collaboration on the Global Brain, ONR MURI,
925 the Klingenstein-Simons Foundation, the Pew Charitable Trust and the Gatsby Charitable
926 Foundation.

Supplemental Figures

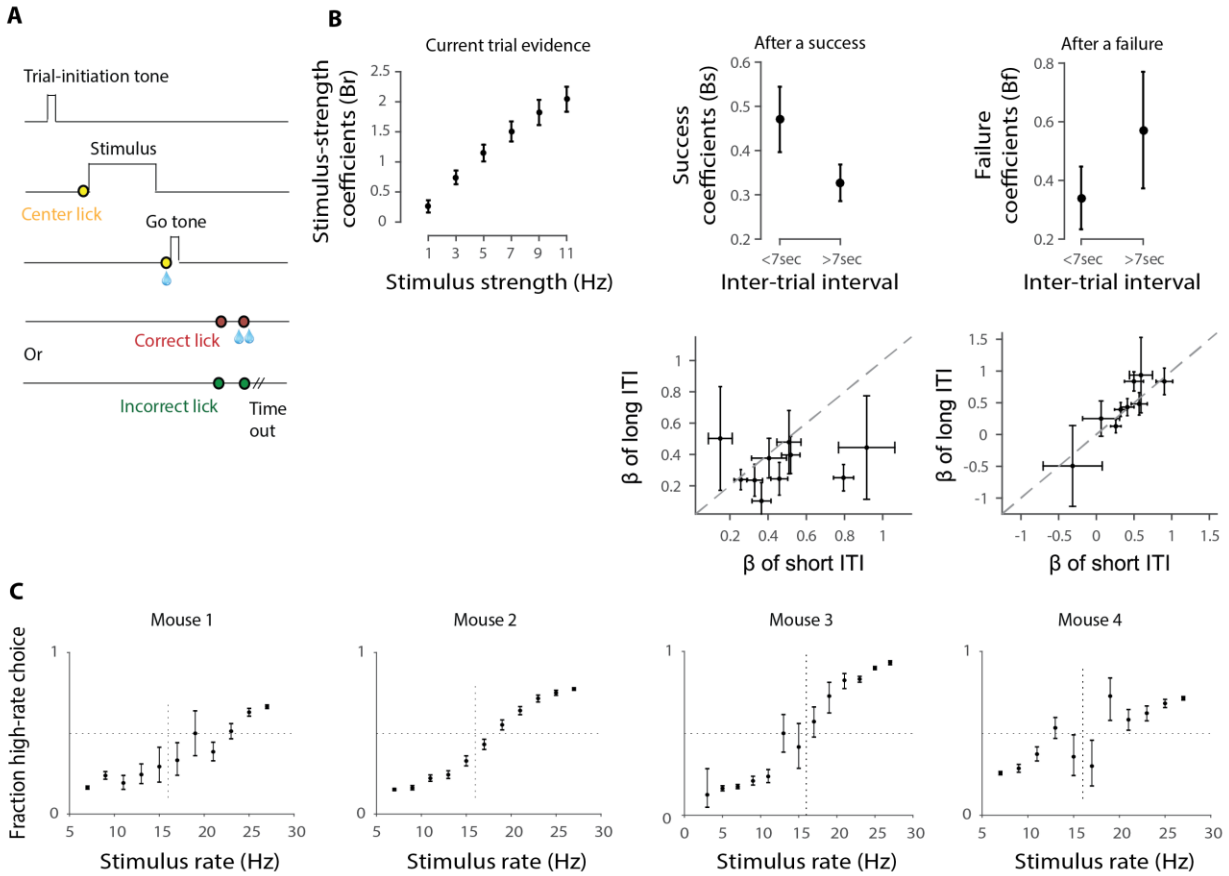


Figure S1. Related to Figure 1. Perceptual decisions about stimulus rate reflect current evidence, previous trial’s outcome, and the time passed since the previous trial.

A, Trial structure. In each trial, first a brief tone is presented to indicate to the animal to initiate the trial (“trial-initiation tone”). Once the animal licks to the center waterspout (row 2: yellow circle), the stimulus is presented for 1 sec. At the end of the stimulus, the animal is required to lick again in the center (row 3: yellow circle). This will result in: 1) a small water reward in the center, 2) a “go tone” that indicates to the animal to make its choice. If the animal licks to the correct side (row 4, 1st red circle), and confirms this lick (row 4, 2nd red circle), it will receive water as a reward. If the animal licks to the wrong side (last row, 1st green circle), and confirms this lick (last row, 2nd green circle), there will be a time-out, i.e. longer time before the next trial can start. **B**, A logistic regression model was used to assess the extent to which the animal’s choice depends on stimulus strength (how far the stimulus rate is from the category boundary at 16Hz), previous choice outcome, and the time interval since the previous trial. Stimulus strength was divided into 6 bins (**left**); previous success was divided into 2 bins: success after a long ITI and success after a short ITI (**middle**); previous failure was also divided into 2 bins: failure after a long ITI and failure after a short ITI (**right**). Plots in top row show β averaged across animals (same 10 animals as in Figure 1B). Error bars: S.E.M across subjects. **Top left**: strength of the sensory evidence affects the animal’s choices: the stronger the evidence, the higher the impact. **Top middle**: Success of a previous trial also affects animal’s decision; the effect is stronger when the previous success occurs after a short ITI (<7sec). **Top Right**: Same but for previous incorrect trials; the effect of ITI after a failure was not significant. Plots in **bottom** row show success (left) and failure (right) β for individual mice. Error bars: S.E.M returned from glmfit.m in Matlab. **C**, Behavioral performance of the four mice in which we imaged excitatory and inhibitory activity during decision-making. In mice 1, 2, and 4, imaging was performed throughout learning by tracking the same group of neurons. Plots reflect data from all sessions. Errors bars: Wilson Binomial Confidence Interval.

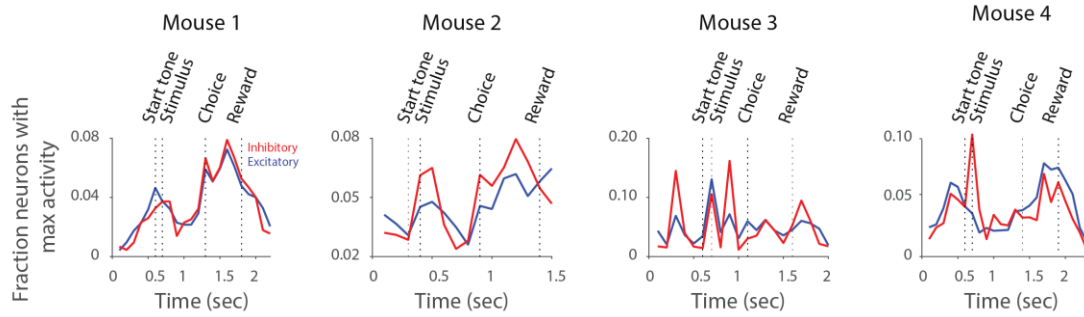


Figure S2. Related to Figure 1. Excitatory and inhibitory neurons have similar temporal dynamics.

For each session, the fraction of neurons with peak activity in each 100ms time window was computed. This quantity is an estimate of the temporal-epoch tuning of neurons. Curves show mean across sessions, for excitatory (blue) and inhibitory (red) neurons, for each mouse. Similar to Figure 1E, traces were aligned for each trial event (start tone, stimulus, choice, reward), and then concatenated (see Figure 1E, legend).

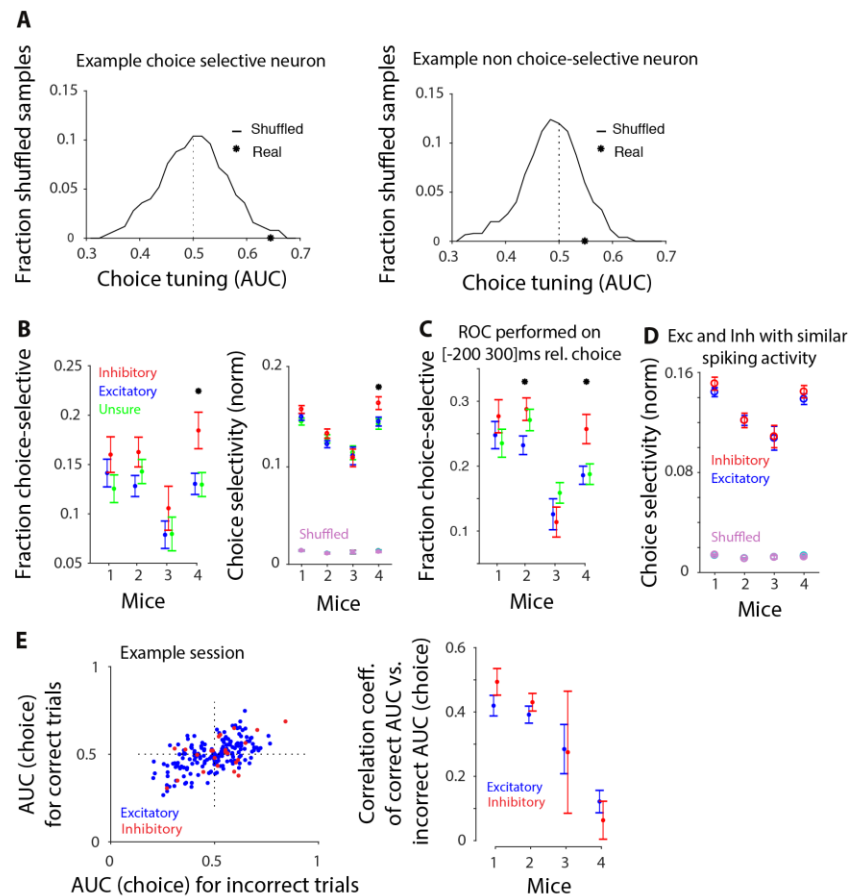


Figure S3. Related to Figure 2. Single neuron measures reveal similar choice selectivity in excitatory and inhibitory neurons.

A, Example neurons to illustrate the method for assessing significant choice selectivity in individual neurons. In both panels, the solid line shows the distribution of values for the area under the ROC curve (AUC) generated by 50 different trial shuffles in which trials were randomly assigned to a left vs. right choice. Star indicates the actual AUC value of the neuron. Significance was assessed from the probability of occurrence of the actual AUC value in the shuffle distribution. When probabilities were <0.05 , neurons were considered choice selective. Only the neuron on the left has significant choice selectivity. **B**, Fraction (left) and magnitude (right) of choice selectivity are shown for the unsure neurons (i.e. neurons classified as neither excitatory nor inhibitory; green), as well as excitatory (blue) and inhibitory (red) neurons. Data for each mouse show mean \pm standard error across sessions. **C**, Fraction of choice-selective neurons based on ROC analysis on [-200 300]ms relative to the choice. Fraction selective neurons at this time window (median across mice): excitatory: 21%; inhibitory: 27%, resulting in approximately 11 inhibitory and 69 excitatory neurons with significant choice selectivity per session. There is a considerable increase in the fraction of selective neurons when using this time window rather than 0-97ms window (see Figure 2C for comparison). **D**, ROC analysis restricted to those excitatory and inhibitory neurons that had the same spiking activity. Choice selectivity is still similar between the two cell types. Note that the significant difference observed for mouse 4 in Figure 2C is absent after controlling for the difference in spiking activity of inhibitory and excitatory neurons. Mean \pm standard error across sessions. **E, left**: Choice selectivity was computed on correct trials (vertical axis) as well as error trials (horizontal axis), and was correlated between the two conditions. Data is from a single session, each point shows an individual neuron whose cell type is indicated by its color. The positive correlation indicates that choice selectivity was overall similar on correct and error trials (Pearson's correlation coefficient, excitatory neurons: $r=0.58$; $p<0.001$; inhibitory neurons: $r=0.55$, $p=0.007$). The small number of points in quadrants 2 and 4 indicate less frequent neurons that showed opposite selectivity on correct vs. error trials. **Right**, Summary of correlation coefficient of AUC on correct trials vs. AUC on incorrect trials, mean across sessions for each animal. Error bars: S.E.M. across sessions. The weaker correlation in mouse 4 indicates that this animal had a mixture of cells selective for the stimulus and cells selective for the choice. Note that although the center of the imaging window was identical in all animals, the imaging location within the window of this animal was slightly posterior to the others. The enrichment of cells selective for the stimulus, in this mouse compared to other mice, may reflect that the region we imaged in mouse 4 was closer to primary visual cortex.

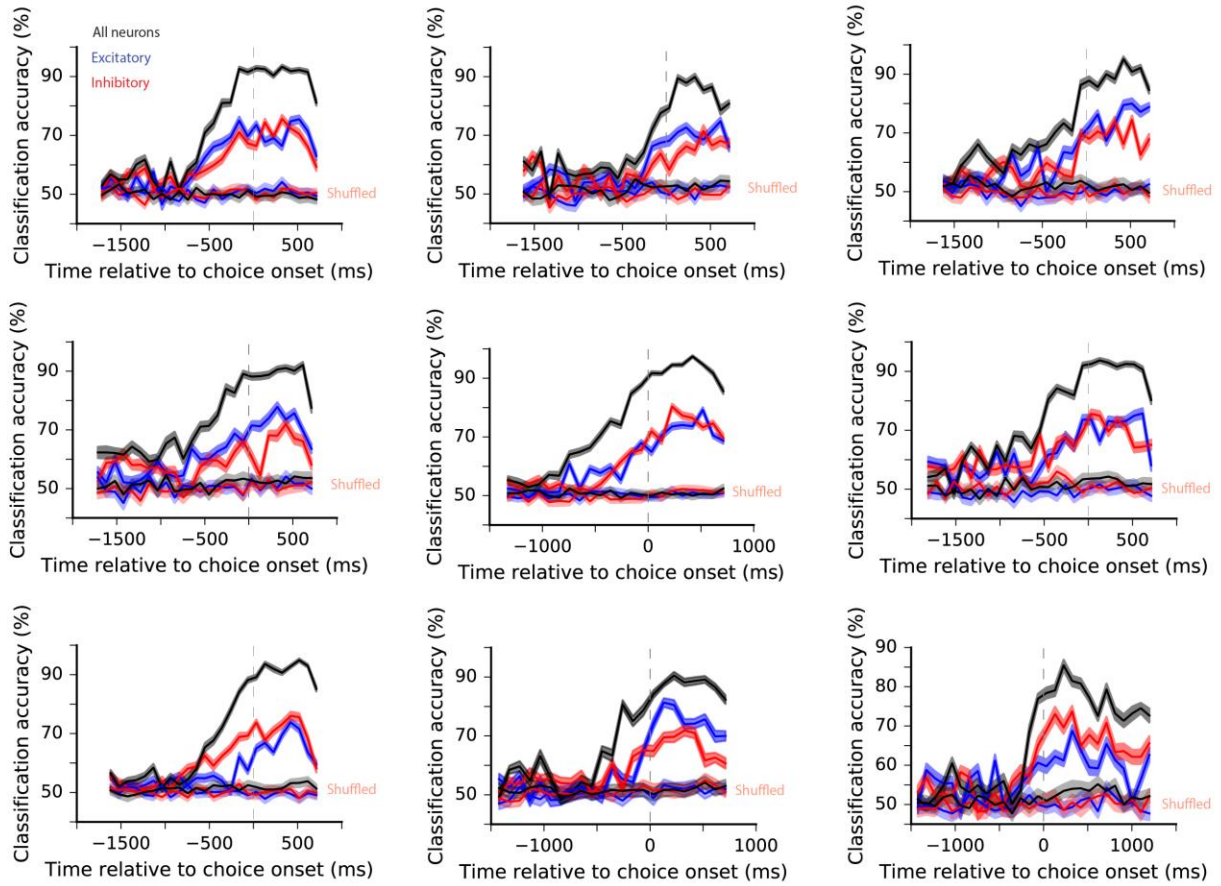


Figure S4. Related to Figure 3. Population activity is highly selective for the animal’s choice; excitatory and inhibitory neurons are similarly selective.

Classification accuracy of the choice decoder at each moment in the trial for 9 additional example sessions. Dashed lines: choice onset. Black: all neurons included in the decoder; blue: subsampled excitatory neurons; red: inhibitory neurons; dim colors: shuffled control. In most sessions, inhibitory and subsampled excitatory populations have comparable classification accuracy.

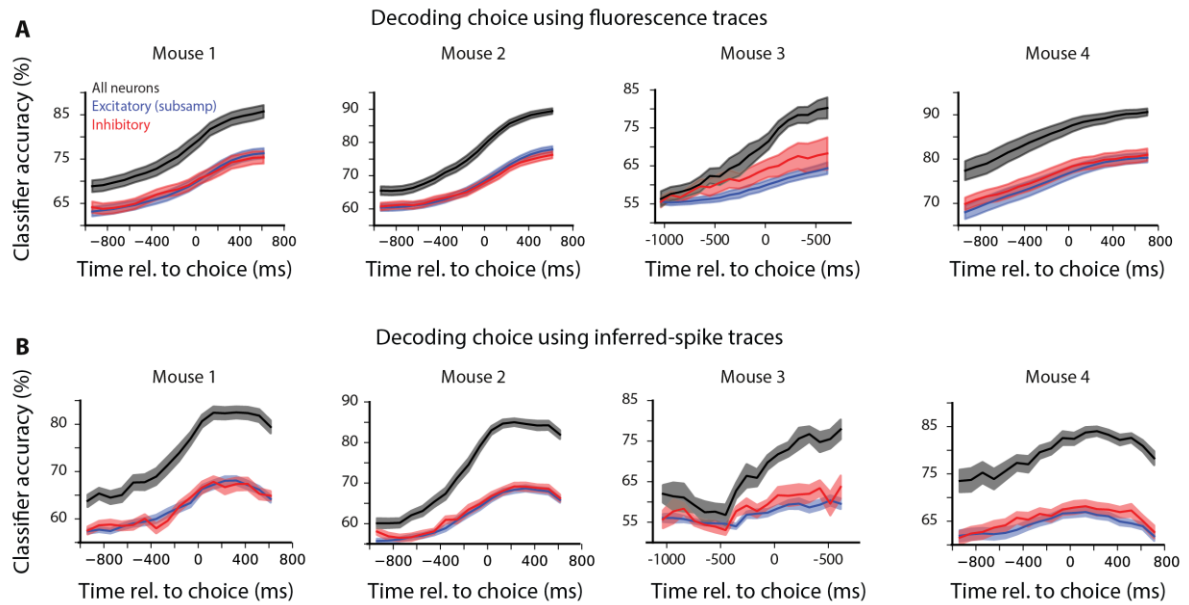


Figure S5. Related to Figure 3. Classification accuracy is similar for excitatory and inhibitory populations, whether the choice decoder is trained/tested on fluorescence traces or on inferred spikes.

SVM classifiers were trained to decode choice from the population activity of all neurons (black), inhibitory neurons (red), or subsampled excitatory neurons (blue). In (A) fluorescence traces (Figure 1D middle) were used, and in (B) inferred spikes (Figure 1D right) were used. In both cases, decoder accuracy is similarly high for excitatory and inhibitory neurons.

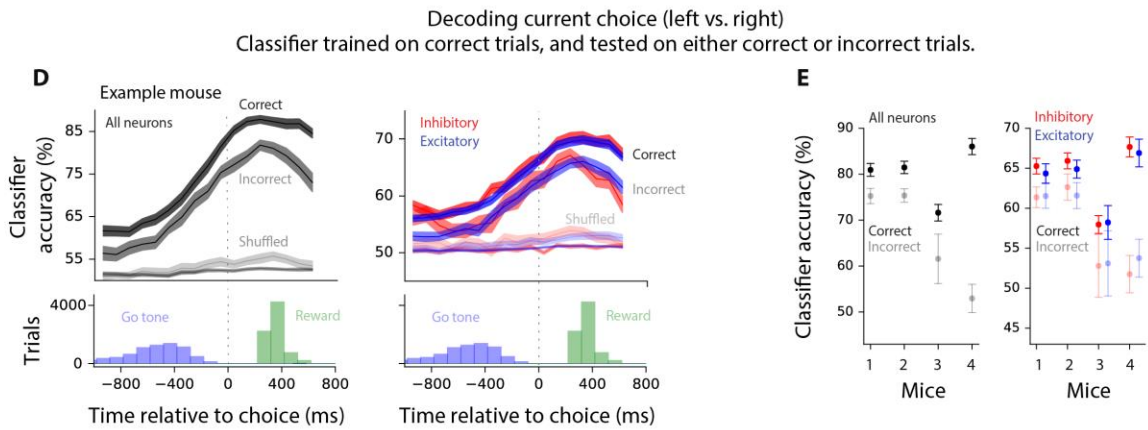
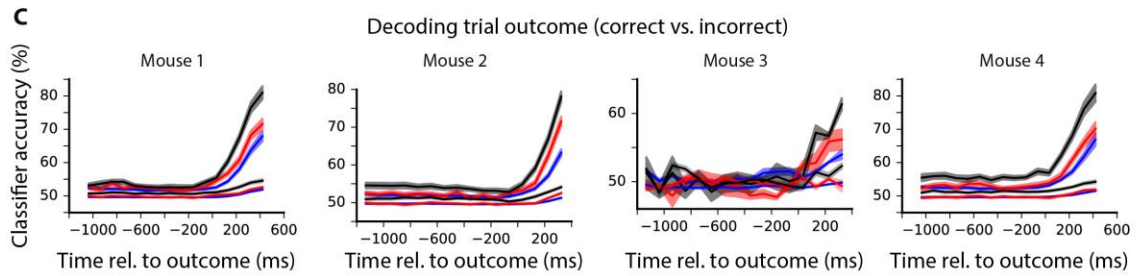
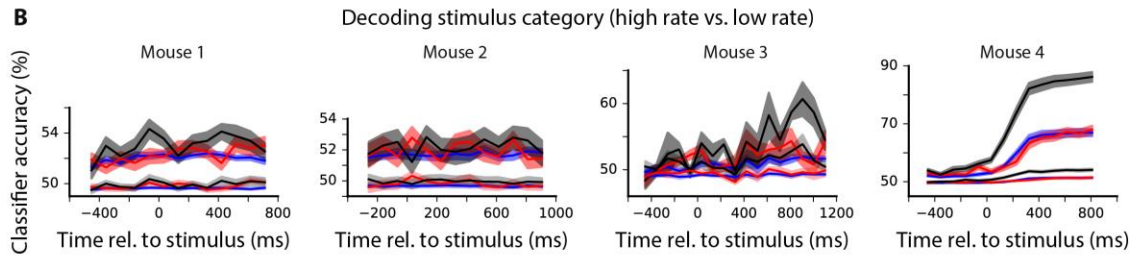
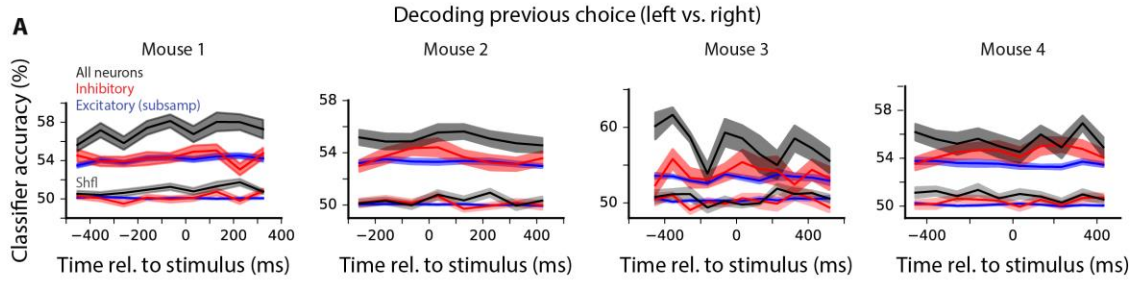


Figure S6. Related to Figure 3. Population activity is strongly selective for the trial outcome, and to a lesser degree to the stimulus category and previous choice.

A, SVM classifier trained to decode previous choice from the activity of all neurons (black), inhibitory neurons (red), or subsampled excitatory (blue) neurons. “shfl” indicates classifier accuracy trained using shuffled trial labels. Previous choice is reflected, though weakly, in the population activity of the current trial. **B**, SVM classifier trained to decode the stimulus category, i.e. whether the stimulus is high rate (above 16Hz) or low rate (below 16Hz). Except for mouse 4, in which the imaging location was slightly more posterior (see Figure S3E, legend), stimulus category is weakly reflected in the population activity. **C**, SVM classifier trained to decode the trial outcome (i.e. correct vs. incorrect). Classification accuracy gradually increases and reaches 80% (median across mice) approximately 400ms after the animal confirms his choice (Figure S1A). Inhibitory neurons showed slightly higher selectivity for the outcome. Unsaturated lines in B and C: performance on shuffled trials. **D**, SVM classifier trained on correct trials to decode choice and tested on correct as well as incorrect trials. Data from an example animal (48 sessions). **Top**: Classification accuracy of decoders trained on all neurons (left), subsampled excitatory neurons (right, blue trace), and inhibitory neurons (right, red trace). In all cases, classifiers were trained on correct trials; however they were tested either on correct (dark lines: “Correct”) or incorrect (dim lines: “Incorrect”) trials. Classification accuracy on incorrect trials was high; indicating that population activity primarily reflects the animal’s choice, yet it differs at least slightly for correct and incorrect trials. This reduction was similar for excitatory and inhibitory neurons (blue and red traces are overlapping in the right panel). **Bottom**: Across-trial distribution of go tones and reward delivery (See Fig. 3B bottom). Left and right panels are the same plots and are duplicated to facilitate alignment to each corresponding plot above. **E**, Summary across all mice for all neurons (left) and excitatory and inhibitory neurons separately (right). Classifier performance on correct (dark colors) and incorrect (dim colors) trials is shown. Mouse 4 had the largest difference in classification accuracy for correct vs. error trials. As with the single-neuron analysis (Figure S3E) and decoding of stimulus category (Figure S6B), this difference likely reflects that the imaging region was slightly posterior within the window for this animal. Importantly, for all mice, the change in classification accuracy was quite similar for excitatory and inhibitory neurons (right), indicating that both populations reflect choice vs. stimulus to a comparable degree.

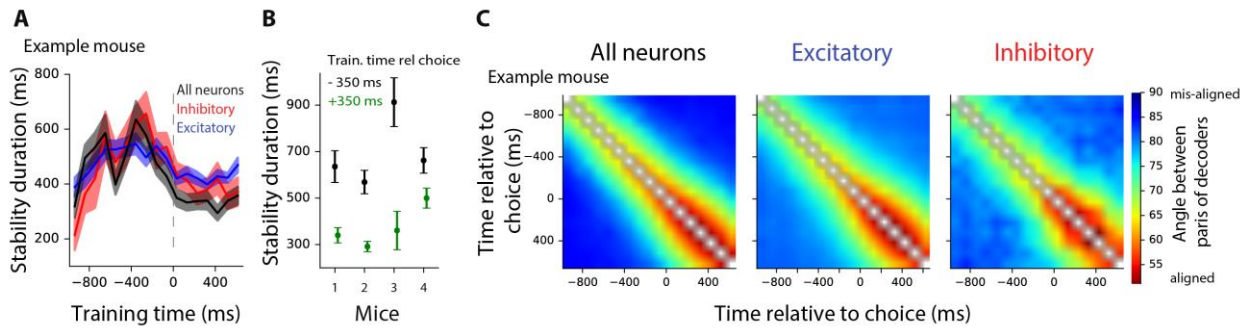


Figure S7. Related to Figure 4. Additional analyses provide more evidence for similar temporal stability of the choice decoder in excitatory and inhibitory populations.

A, In an example mouse, population activity that predicts the animal’s choice is similarly stable for excitatory and inhibitory neurons during the course of a trial. The vertical axis shows the stability duration for decoders trained at different times during the trial. Stability duration is defined as the width of the testing window over which decoder accuracy does not statistically differ from that within the training window (red regions of Figure 4C) from that obtained by using the same training and testing times (diagonal of Figure 4A). Error bars: S.E.M. across sessions. Summary data for all mice at training time 0-97 ms before choice (dashed line) are shown in Figure 4D. **B**, Stability duration of the all-neuron decoder (black in panel A) is compared for decoders trained 350ms before the choice (black), and 350ms after the choice (green). Population stability was lower after the choice than before the choice. This may be due to additional events, e.g. reward delivery and repeated licking, which follow the choice. **C**, Another measurement of stability likewise suggests similar temporal stability for excitatory and inhibitory populations. Stability was assessed by measuring the angle between pairs of decoders trained at different time points in the trial. If a similar pattern of population activity represents choice from moment t_1 to moment t_2 , the choice classifiers trained at these times will be aligned, i.e. the angle between the two classifiers will be small. The colors indicate the angle between pairs of decoders trained at different moments in the trial. Small angles (hot colors) indicate alignment of choice decoders; hence stable activity patterns, related to choice, across neurons. Left: all neurons; middle: excitatory neurons (subsampling to match the number of inhibitory neurons); right: inhibitory neurons. As with our other method (Figure 4), the time course of stability was similar for excitatory and inhibitory neurons.

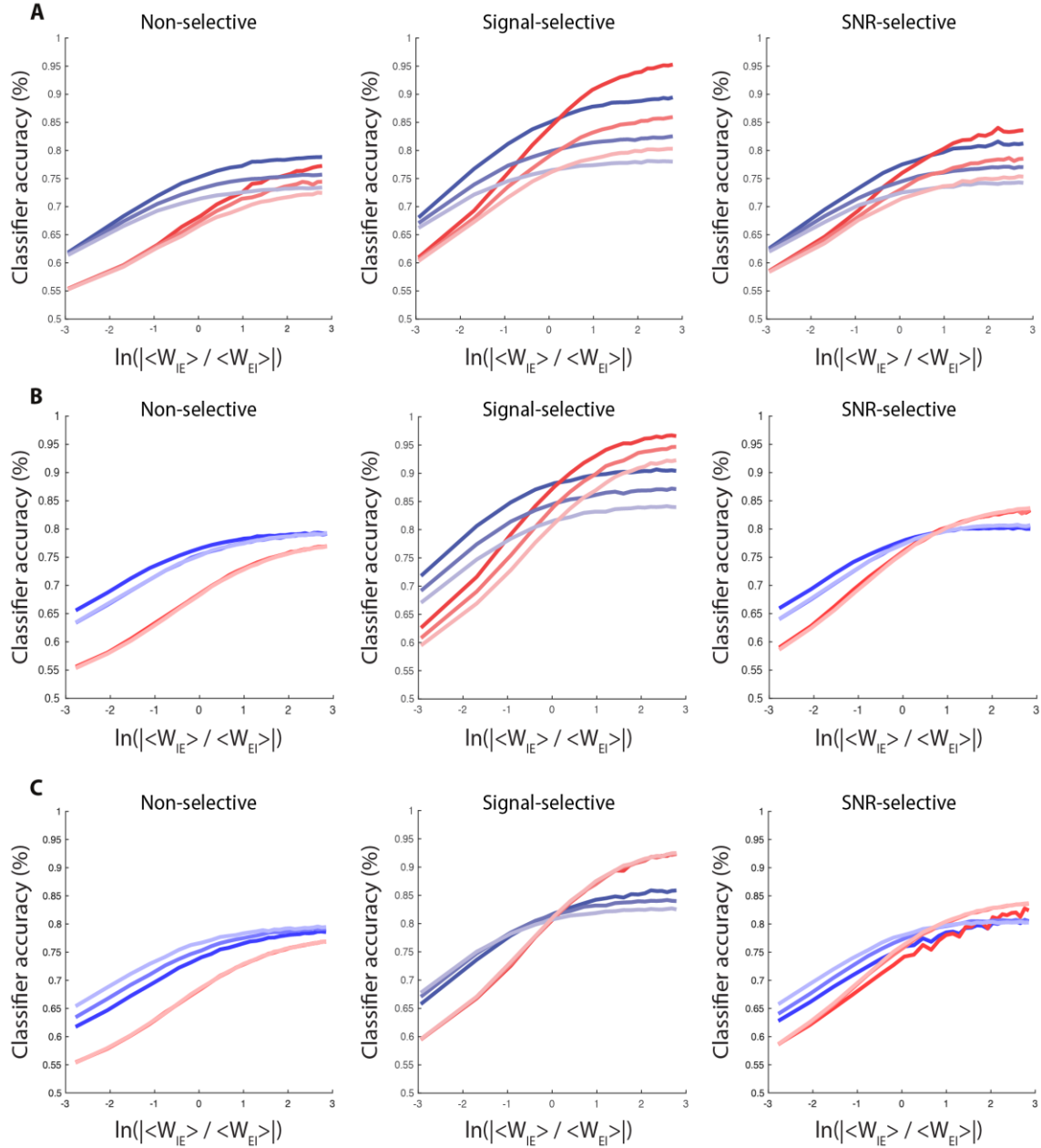


Figure S8. Related to Figure 5. Selective connectivity between excitatory and inhibitory neurons allows for matched classification accuracy in the two populations.

Decoding accuracy versus three parameters. **A**, Differential correlations, which are known to be present in any realistic network (Moreno-Bote et al., 2014). $\Sigma_{EE} \rightarrow \Sigma_{EE} + \epsilon \Delta \mathbf{h} \Delta \mathbf{h}$. Dark to light hues: $\epsilon = 0, 0.25, 0.50$. **B**, Excitatory to excitatory connections. Dark to light hues: $w_{EE} = 0.35, 0.3, 0.25$ (default). **C**, Inhibitory to inhibitory connections. Dark to light hues: $w_{II} = -2.4, -2.0$ (default), and -1.6 .

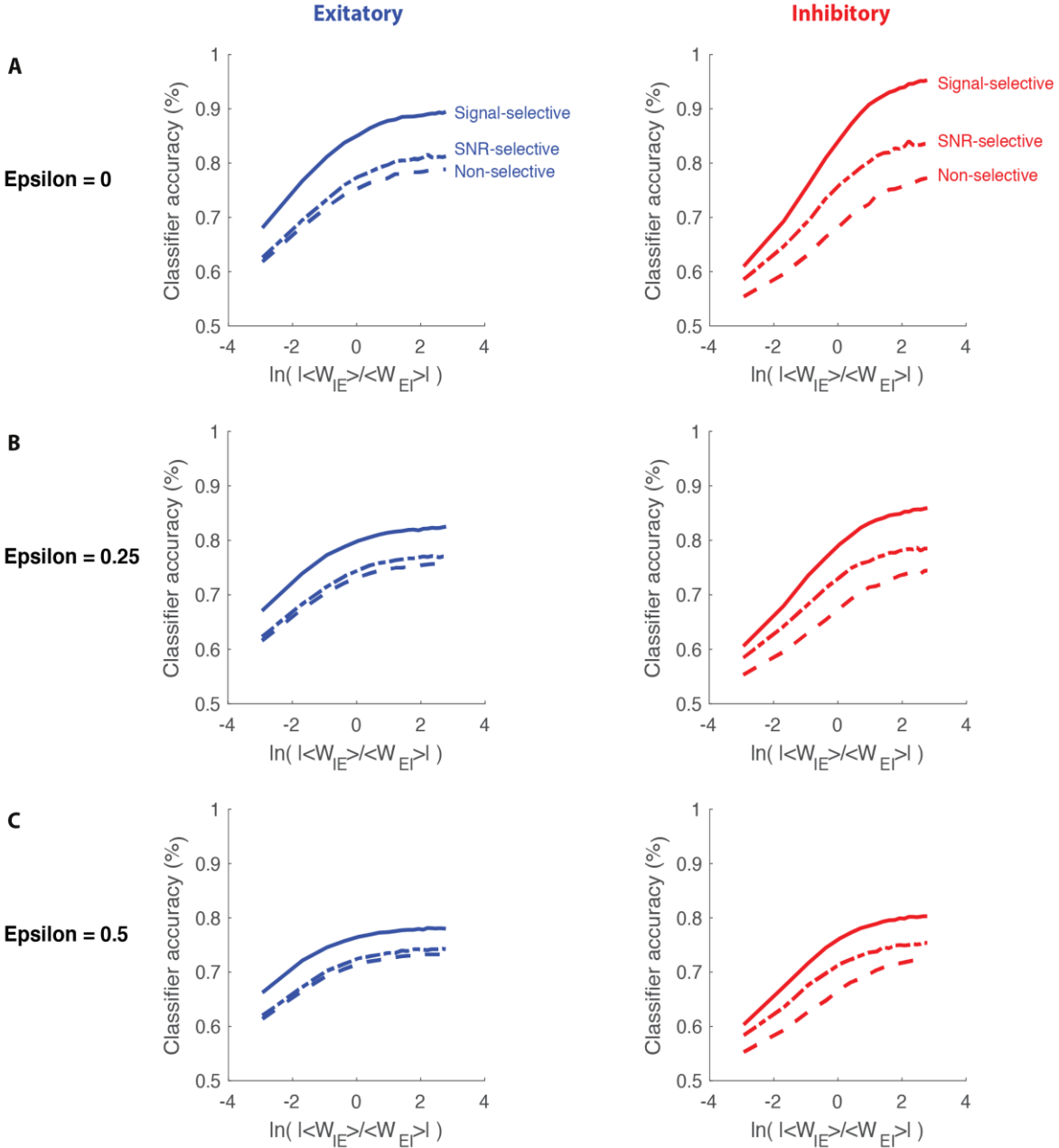


Figure S9. Related to Figure 5. Signal-selective models of decision-making have significantly higher classification accuracy compared to non-selective and SNR-selective models.

Classification accuracy of excitatory (blue) and inhibitory (red) neurons is compared for 3 models of decision-making with different levels of differential correlations, as controlled by ϵ (see Fig. 8 caption). We focused on differential correlations because they are known to be present in any realistic network (Moreno-Bote et al., 2014). Solid: signal-selective; Dashed-dotted: SNR-selective; Dashed: non-selective. **A**, **B**, **C**: $\epsilon = 0, 0.25, 0.50$, respectively. Horizontal axis shows the relative strength of excitatory-to-inhibitory vs. inhibitory-to-excitatory connections. For all values of this parameter and in both cell types, signal-selective model has the highest classification accuracy for decoding the animal's choice.

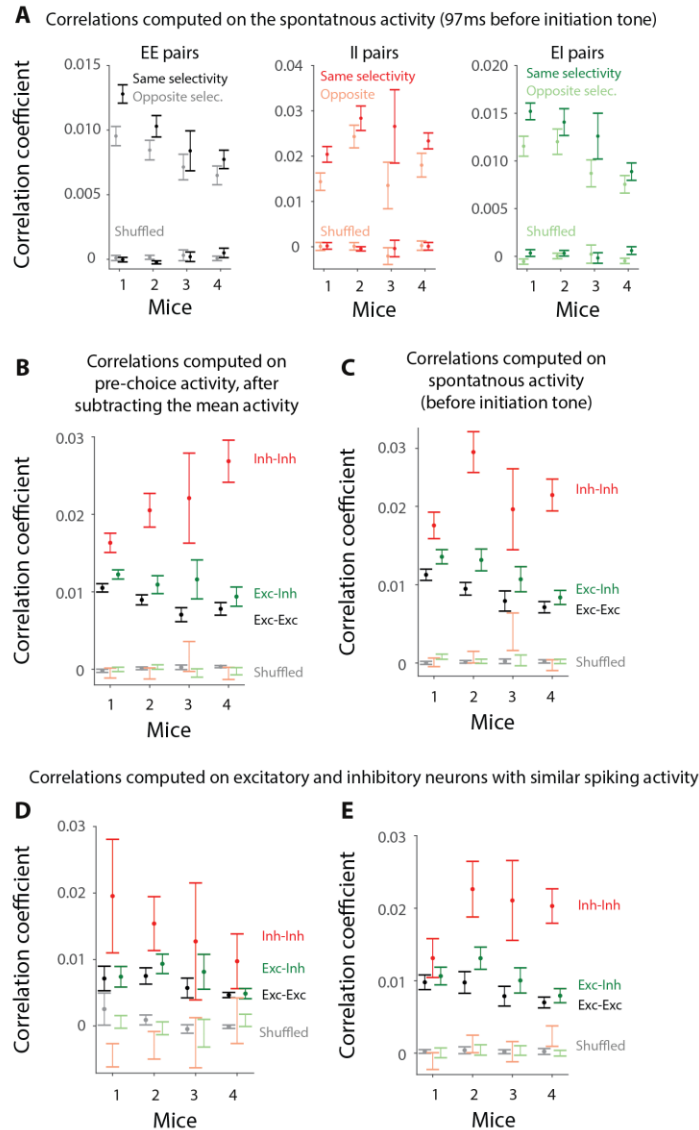


Figure S10. Related to Figure 6. Higher noise correlations between neurons with similar choice selectivity. Also, inhibitory neurons are more strongly correlated.

A, Noise correlations between neurons with the same choice selectivity (dark colors) vs. those with opposite choice selectivity (dim colors), for pairs of excitatory neurons (left), pairs of inhibitory neurons (middle) or excitatory-inhibitory pairs (right). Signal correlations were not present because correlations were computed 0-97 ms before the trial initiation tone, when the stimulus is not present, and the activity is spontaneous. **B**, Noise correlations were much stronger for inhibitory-inhibitory pairs (red) than excitatory-excitatory pairs (black), and had intermediate values for excitatory-inhibitory pairs (green). Correlations are computed on 0-97ms before the choice after subtracting off the mean choice activity, hence removing the signal correlations. **C**, Same as B but for the time period 0-97 ms before the trial initiation tone (i.e. the spontaneous activity). **D,E**, same as in B,C, except correlations were computed only on those excitatory and inhibitory neurons with the same median spiking activity (Methods).

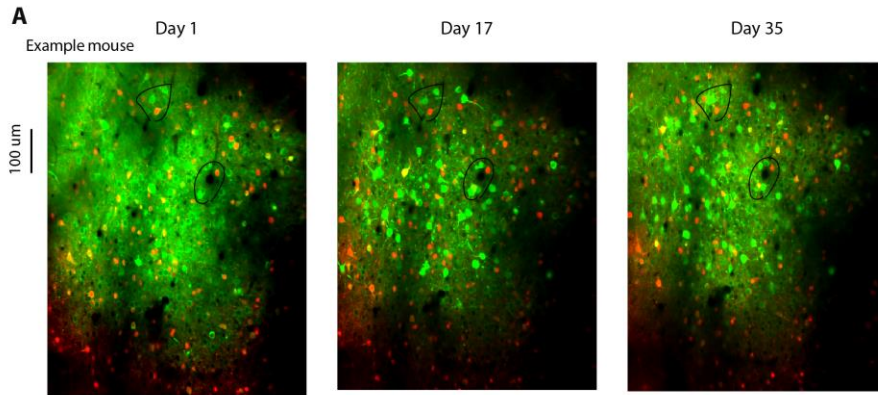


Figure S11. Related to Figure 8. The same field of view was imaged during learning.

A, Field of view from three example sessions of a mouse: 1st days of imaging (left), a middle imaging session (middle), and last day of imaging (right). Left to right panels span 60 days, out of which 35 days were experimental days. Black circles mark example areas that can be easily matched among the sessions. Each panel is an average image of all the frames imaged in the session. Green and red (bleedthrough corrected) images were merged.

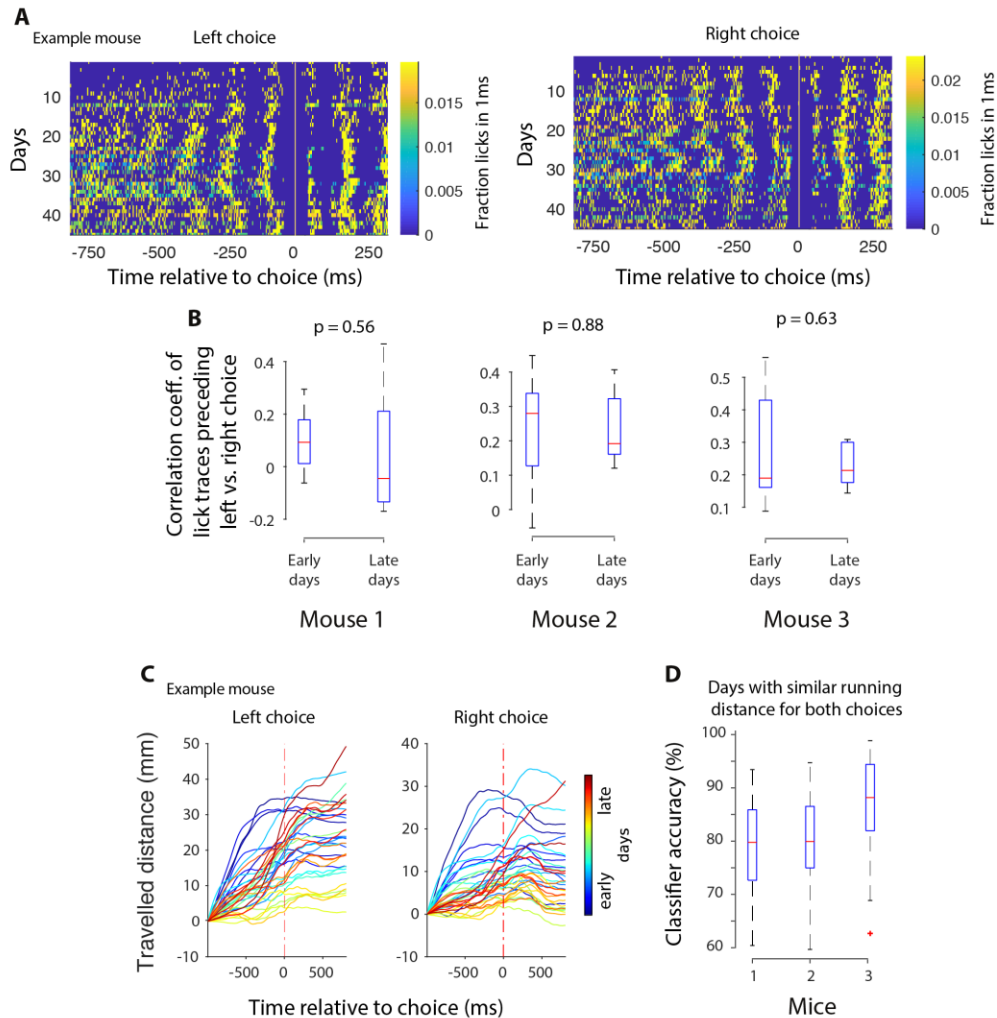


Figure S12. Related to Figure 8. Further analysis of learning-induced changes in the population activity: changes in licking and running movements are unlikely to account for improved classifier accuracy during learning.

A, Licking was similar in advance of high rate vs. low rate choices, both early and late in training. Licks that occur before the choice (vertical line at 0) are to the center waterspout, and licks that occur after the choice are to the side waterspouts; example mouse. **B**, Each plot shows the Pearson's correlation coefficient between licking patterns, to the center waterspout, preceding left and right choices, calculated 250ms before the choice. These correlations were typically similar for early vs. late training days, indicating that animal's licking pattern preceding left vs. right choices did not change drastically over the course of learning. **C**, Distance that the animal travelled during the decision (as measured by the rotary encoder on the running wheel) was similar in advance of left vs. right choices; example mouse; each line represents a session (cold colors: early sessions; hot colors: late sessions). **D**, Classifier accuracy (0-97 ms before the choice) of the full population was high even when the analysis was restricted to sessions in which the distance travelled was not significantly different (t-test, $P > 0.05$; time 0-97 ms before the choice) for left vs. right choices. This analysis was necessary because for some mice in some sessions, there were idiosyncratic differences between the distances travelled in advance of left vs. right choices. In (B) and (D), median (red horizontal line), inter-quartile range (blue box), and the entire range of data (dashed black lines) are shown. There is a single red '+' at the bottom of mouse 3. What is the story there?

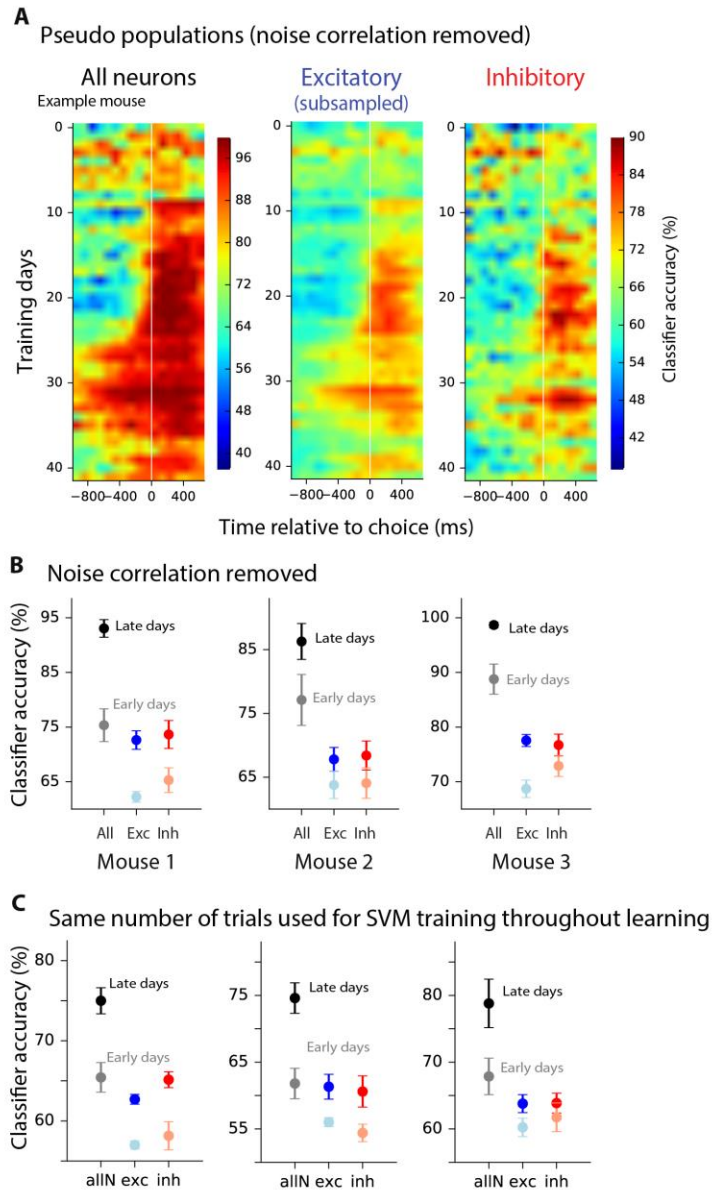


Figure S13. Related to Figure 8. Further analysis of learning-induced changes in the population activity: the reduction in noise correlations is insufficient to account for the improved classification accuracy during learning. Instead, the improvement can be explained by an increase in the fraction of significantly choice-selective neurons. A, Classification accuracy for each training session (average of cross-validation samples), for all neurons (left), subsampled excitatory (middle), and inhibitory neurons (right); example mouse. White vertical line: choice onset. This format is the same as Figure 8A, but here the noise correlations are removed by making pseudo populations (similar procedure as in Figure 7). **B,** Summary of each mouse, showing classification accuracy averaged across early (unsaturated colors) vs. late (saturated colors) training days, at 0-97ms before the choice. As in (A), data are based on pseudo-populations in which the noise correlations are removed. The learning-induced improvement in the classifier accuracy in pseudo populations indicates that reduced noise correlations (Figure 8F) cannot solely account for the enhanced classifier accuracy in the population during learning (Figure 8A). **C,** Equal trial numbers were used to train the choice classifier in every session to control for any effects of trial numbers on classifier accuracy. An increase in classifier accuracy is still observed as a result of learning. Classifiers were trained only on correct trials.

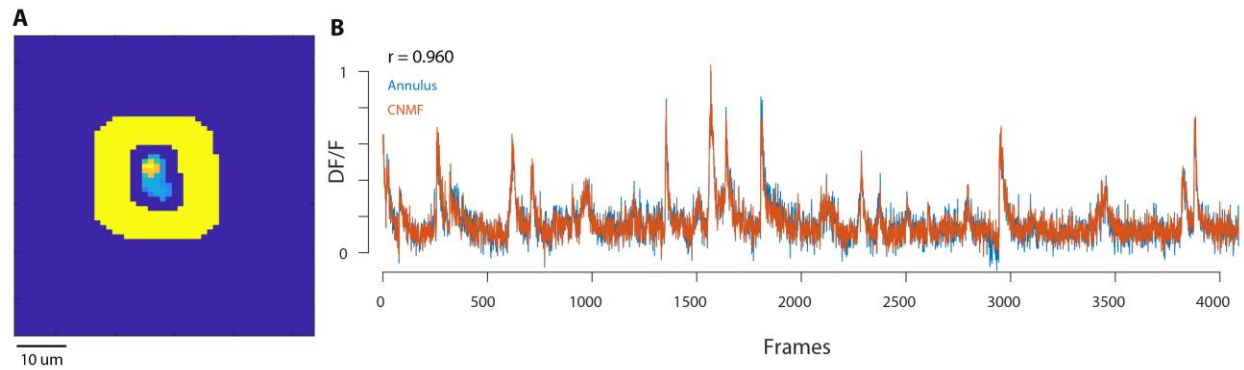


Figure S14. Related to Methods section “Neuropil Contamination removal”. Removing neuropil contamination with CNMF or manually using an annulus leads to the same results.

A, An example spatial component in the FOV and its surrounding annulus (yellow). **B**, $\Delta F/F$ trace for the same component obtained by manually subtracting the neuropil activity averaged over the annulus region (blue trace) or by using the output of the CNMF processing pipeline (red trace). The two traces look nearly identical as also demonstrated by their high correlation coefficient ($r = 0.96$; the traces are not denoised). These results demonstrate the ability of the CNMF framework to properly capture neuropil contamination and remove it from the detected calcium traces.

References

- 927 Akrami A, Kopec CD, Diamond ME, Brody CD (2018) Posterior parietal cortex represents
928 sensory history and mediates its effects on behaviour. *Nature* 554:368-372.
- 929 Allen WE, Kauvar IV, Chen MZ, Richman EB, Yang SJ, Chan K, Gradinaru V, Deverman BE,
930 Luo L, Deisseroth K (2017) Global Representations of Goal-Directed Behavior in
931 Distinct Cell Types of Mouse Neocortex. *Neuron* 94:891-907 e896.
- 932 Atallah BV, Bruns W, Carandini M, Scanziani M (2012) Parvalbumin-expressing interneurons
933 linearly transform cortical responses to visual stimuli. *Neuron* 73:159-170.
- 934 Averbeck BB, Lee D (2006) Effects of noise correlations on information encoding and decoding.
935 *J Neurophysiol* 95:3633-3644.
- 936 Averbeck BB, Latham PE, Pouget A (2006) Neural correlations, population coding and
937 computation. *Nat Rev Neurosci* 7:358-366.
- 938 Beaulieu C (1993) Numerical data on neocortical neurons in adult rat, with special reference to
939 the GABA population. *Brain Res* 609:284-292.
- 940 Beck JM, Ma WJ, Kiani R, Hanks T, Churchland AK, Roitman J, Shadlen MN, Latham PE,
941 Pouget A (2008) Probabilistic population codes for Bayesian decision making. *Neuron*
942 60:1142-1152.
- 943 Bock DD, Lee WC, Kerlin AM, Andermann ML, Hood G, Wetzel AW, Yurgenson S, Soucy ER,
944 Kim HS, Reid RC (2011) Network anatomy and in vivo physiology of visual cortical
945 neurons. *Nature* 471:177-182.
- 946 Bogacz R, Brown E, Moehlis J, Holmes P, Cohen JD (2006) The physics of optimal decision
947 making: a formal analysis of models of performance in two-alternative forced-choice
948 tasks. *Psychol Rev* 113:700-765.
- 949 Brunton BW, Botvinick MM, Brody CD (2013) Rats and humans can optimally accumulate
950 evidence for decision-making. *Science* 340:95-98.
- 951 Busse L, Ayaz A, Dhruv NT, Katzner S, Saleem AB, Scholvinck ML, Zaharia AD, Carandini M
952 (2011) The detection of visual contrast in the behaving mouse. *J Neurosci* 31:11351-
953 11361.
- 954 Ch'ng YH, Reid RC (2010) Cellular imaging of visual cortex reveals the spatial and functional
955 organization of spontaneous activity. *Front Integr Neurosci* 4.
- 956 Chen TW, Wardill TJ, Sun Y, Pulver SR, Renninger SL, Baohan A, Schreiter ER, Kerr RA,
957 Orger MB, Jayaraman V, Looger LL, Svoboda K, Kim DS (2013) Ultrasensitive
958 fluorescent proteins for imaging neuronal activity. *Nature* 499:295-300.
- 959 Constantinidis C, Goldman-Rakic PS (2002) Correlated discharges among putative pyramidal
960 neurons and interneurons in the primate prefrontal cortex. *J Neurophysiol* 88:3487-3497.
- 961 Cossell L, Iacaruso MF, Muir DR, Houlton R, Sader EN, Ko H, Hofer SB, Mrsic-Flogel TD
962 (2015) Functional organization of excitatory synaptic strength in primary visual cortex.
963 *Nature* 518:399-403.
- 964 de Lima AD, Voigt T (1997) Identification of two distinct populations of gamma-aminobutyric
965 acidergic neurons in cultures of the rat cerebral cortex. *J Comp Neurol* 388:526-540.
- 966 de Lima AD, Gieseler A, Voigt T (2009) Relationship between GABAergic interneurons
967 migration and early neocortical network activity. *Dev Neurobiol* 69:105-123.
- 968 Deneve S, Latham PE, Pouget A (1999) Reading population codes: a neural implementation of
969 ideal observers. *Nat Neurosci* 2:740-745.

970 Driscoll LN, Pettit NL, Minderer M, Chettih SN, Harvey CD (2017) Dynamic Reorganization of
971 Neuronal Activity Patterns in Parietal Cortex. *Cell* 170:986-999 e916.

972 Ego-Stengel V, Wilson MA (2007) Spatial selectivity and theta phase precession in CA1
973 interneurons. *Hippocampus* 17:161-174.

974 Elsayed GF, Lara AH, Kaufman MT, Churchland MM, Cunningham JP (2016) Reorganization
975 between preparatory and movement population responses in motor cortex. *Nat Commun*
976 7:13239.

977 Francis NA, Winkowski DE, Sheikhattar A, Armengol K, Babadi B, Kanold PO (2018) Small
978 Networks Encode Decision-Making in Primary Auditory Cortex. *Neuron* 97:885-897
979 e886.

980 Freedman DJ, Assad JA (2006) Experience-dependent representation of visual categories in
981 parietal cortex. *Nature* 443:85-88.

982 Funamizu A, Kuhn B, Doya K (2016) Neural substrate of dynamic Bayesian inference in the
983 cerebral cortex. *Nat Neurosci* 19:1682-1689.

984 Gabbott PL, Dickie BG, Vaid RR, Headlam AJ, Bacon SJ (1997) Local-circuit neurones in the
985 medial prefrontal cortex (areas 25, 32 and 24b) in the rat: morphology and quantitative
986 distribution. *J Comp Neurol* 377:465-499.

987 Galarreta M, Hestrin S (1999) A network of fast-spiking cells in the neocortex connected by
988 electrical synapses. *Nature* 402:72-75.

989 Giovannucci A, Friedrich J, Gunn P, Kalfon J, Koay SA, Taxidis J, Najafi F, Gauthier JL, Zhou
990 P, Tank DW, Chklovskii DB, Pnevmatikakis EA (2018) CaImAn: An open source tool
991 for scalable Calcium Imaging data Analysis. *bioRxiv*.

992 Giovannucci A, Friedrich J, Gunn P, Kalfon J, Brown BL, Koay SA, Taxidis J, Najafi F,
993 Gauthier JL, Zhou P, Khakh BS, Tank DW, Chklovskii DB, Pnevmatikakis EA (2019)
994 CaImAn an open source tool for scalable calcium imaging data analysis. *Elife* 8.

995 Goard MJ, Pho GN, Woodson J, Sur M (2016) Distinct roles of visual, parietal, and frontal
996 motor cortices in memory-guided sensorimotor decisions. *Elife* 5.

997 Green DM, Swets JA (1966) Signal detection theory and psychophysics. New York: Wiley.

998 Gu Y, Liu S, Fetsch CR, Yang Y, Fok S, Sunkara A, DeAngelis GC, Angelaki DE (2011)
999 Perceptual learning reduces interneuronal correlations in macaque visual cortex. *Neuron*
1000 71:750-761.

1001 Guizar-Sicairos M, Thurman ST, Fienup JR (2008) Efficient subpixel image registration
1002 algorithms. *Opt Lett* 33:156-158.

1003 Harvey CD, Coen P, Tank DW (2012) Choice-specific sequences in parietal cortex during a
1004 virtual-navigation decision task. *Nature* 484:62-68.

1005 Helmchen F, Tank DW (2019) A Single-Compartment Model of Calcium Dynamics in Nerve
1006 Terminals and Dendrites. *Cold Spring Harb Protoc*; doi:101101/pdbtop085910.

1007 Hofer SB, Ko H, Pichler B, Vogelstein J, Ros H, Zeng H, Lein E, Lesica NA, Mrcic-Flogel TD
1008 (2011) Differential connectivity and response dynamics of excitatory and inhibitory
1009 neurons in visual cortex. *Nat Neurosci* 14:1045-1052.

1010 Hofmann T, Scholkopf B, Smola AJ (2008) Kernel methods in machine learning. *Ann Statist*
1011 36:1171-1220.

1012 Hwang EJ, Dahlen JE, Mukundan M, Komiyama T (2017) History-based action selection bias in
1013 posterior parietal cortex. *Nat Commun* 8:1242.

1014 Isaacson JS, Scanziani M (2011) How inhibition shapes cortical activity. *Neuron* 72:231-243.

1015 Jeanne JM, Sharpee TO, Gentner TQ (2013) Associative learning enhances population coding by
1016 inverting interneuronal correlation patterns. *Neuron* 78:352-363.

1017 Jouhanneau JS, Kremkow J, Poulet JFA (2018) Single synaptic inputs drive high-precision
1018 action potentials in parvalbumin expressing GABA-ergic cortical neurons in vivo. *Nat*
1019 *Commun* 9:1540.

1020 Jouhanneau JS, Kremkow J, Dornn AL, Poulet JF (2015) In Vivo Monosynaptic Excitatory
1021 Transmission between Layer 2 Cortical Pyramidal Neurons. *Cell Rep* 13:2098-2106.

1022 Kamigaki T, Dan Y (2017) Delay activity of specific prefrontal interneuron subtypes modulates
1023 memory-guided behavior. *Nat Neurosci* 20:854-863.

1024 Kerlin AM, Andermann ML, Berezovskii VK, Reid RC (2010) Broadly tuned response
1025 properties of diverse inhibitory neuron subtypes in mouse visual cortex. *Neuron* 67:858-
1026 871.

1027 Khan AG, Poort J, Chadwick A, Blot A, Sahani M, Mrcic-Flogel TD, Hofer SB (2018) Distinct
1028 learning-induced changes in stimulus selectivity and interactions of GABAergic
1029 interneuron classes in visual cortex. *Nature Neuroscience*.

1030 Kim Y, Yang GR, Pradhan K, Venkataraju KU, Bota M, Garcia Del Molino LC, Fitzgerald G,
1031 Ram K, He M, Levine JM, Mitra P, Huang ZJ, Wang XJ, Osten P (2017) Brain-wide
1032 Maps Reveal Stereotyped Cell-Type-Based Cortical Architecture and Subcortical Sexual
1033 Dimorphism. *Cell* 171:456-469 e422.

1034 Kimmel D, Elsayed GF, Cunningham JP, Rangel A, Newsome WT (2016) Encoding of value
1035 and choice as separable, dynamic neural dimensions in orbitofrontal cortex. *Cosyne*.

1036 Ko H, Hofer SB, Pichler B, Buchanan KA, Sjöström PJ, Mrcic-Flogel TD (2011) Functional
1037 specificity of local synaptic connections in neocortical networks. *Nature* 473:87-91.

1038 Krishna VR, Alexander KR, Peachey NS (2002) Temporal properties of the mouse cone
1039 electroretinogram. *J Neurophysiol* 87:42-48.

1040 Kwan AC, Dan Y (2012) Dissection of cortical microcircuits by single-neuron stimulation in
1041 vivo. *Curr Biol* 22:1459-1467.

1042 Law CT, Gold JI (2008) Neural correlates of perceptual learning in a sensory-motor, but not a
1043 sensory, cortical area. *Nat Neurosci* 11:505-513.

1044 Lee WC, Bonin V, Reed M, Graham BJ, Hood G, Glattfelder K, Reid RC (2016) Anatomy and
1045 function of an excitatory network in the visual cortex. *Nature* 532:370-374.

1046 Lim S, Goldman MS (2013) Balanced cortical microcircuitry for maintaining information in
1047 working memory. *Nat Neurosci* 16:1306-1314.

1048 Liu BH, Li P, Li YT, Sun YJ, Yanagawa Y, Obata K, Zhang LI, Tao HW (2009) Visual
1049 receptive field structure of cortical inhibitory neurons revealed by two-photon imaging
1050 guided recording. *J Neurosci* 29:10520-10532.

1051 Lo CC, Wang XJ (2006) Cortico-basal ganglia circuit mechanism for a decision threshold in
1052 reaction time tasks. *Nat Neurosci* 9:956-963.

1053 Lovett-Barron M, Kaifosh P, Kheirbek MA, Danielson N, Zaremba JD, Reardon TR, Turi GF,
1054 Hen R, Zemelman BV, Losonczy A (2014) Dendritic inhibition in the hippocampus
1055 supports fear learning. *Science* 343:857-863.

1056 Ma WP, Liu BH, Li YT, Huang ZJ, Zhang LI, Tao HW (2010) Visual representations by cortical
1057 somatostatin inhibitory neurons--selective but with weak and delayed responses. *J*
1058 *Neurosci* 30:14371-14379.

1059 Machado TA, Pnevmatikakis E, Paninski L, Jessell TM, Miri A (2015) Primacy of Flexor
1060 Locomotor Pattern Revealed by Ancestral Reversion of Motor Neuron Identity. *Cell*
1061 162:338-350.

1062 Machens CK, Romo R, Brody CD (2005) Flexible control of mutual inhibition: a neural model
1063 of two-interval discrimination. *Science* 307:1121-1124.

1064 Madisen L, Zwingman TA, Sunkin SM, Oh SW, Zariwala HA, Gu H, Ng LL, Palmiter RD,
1065 Hawrylycz MJ, Jones AR, Lein ES, Zeng H (2010) A robust and high-throughput Cre
1066 reporting and characterization system for the whole mouse brain. *Nat Neurosci* 13:133-
1067 140.

1068 Marbach F, Zador AM (2017) A self-initiated two-alternative forced choice paradigm for head-
1069 fixed mice. *bioRxiv*.

1070 Maurer AP, Cowen SL, Burke SN, Barnes CA, McNaughton BL (2006) Phase precession in
1071 hippocampal interneurons showing strong functional coupling to individual pyramidal
1072 cells. *J Neurosci* 26:13485-13492.

1073 Mi Y, Katkov M, Tsodyks M (2017) Synaptic Correlates of Working Memory Capacity. *Neuron*
1074 93:323-330.

1075 Moore AK, Wehr M (2013) Parvalbumin-expressing inhibitory interneurons in auditory cortex
1076 are well-tuned for frequency. *J Neurosci* 33:13713-13723.

1077 Morcos AS, Harvey CD (2016) History-dependent variability in population dynamics during
1078 evidence accumulation in cortex. *Nat Neurosci* 19:1672-1681.

1079 Moreno-Bote R, Beck J, Kanitscheider I, Pitkow X, Latham P, Pouget A (2014) Information-
1080 limiting correlations. *Nat Neurosci* 17:1410-1417.

1081 Ni AM, Ruff DA, Alberts JJ, Symmonds J, Cohen MR (2018) Learning and attention reveal a
1082 general relationship between population activity and behavior. *Science* 359:463-465.

1083 Niell CM, Stryker MP (2008) Highly selective receptive fields in mouse visual cortex. *J*
1084 *Neurosci* 28:7520-7536.

1085 Odoemene O, Pisupati S, Nguyen H, Churchland AK (2017) Visual evidence accumulation
1086 guides decision-making in unrestrained mice. *bioRxiv*.

1087 Packer AM, Yuste R (2011) Dense, unspecific connectivity of neocortical parvalbumin-positive
1088 interneurons: a canonical microcircuit for inhibition? *J Neurosci* 31:13260-13271.

1089 Panzeri S, Schultz SR, Treves A, Rolls ET (1999) Correlations and the encoding of information
1090 in the nervous system. *Proc Biol Sci* 266:1001-1012.

1091 Pfeffer CK, Xue M, He M, Huang ZJ, Scanziani M (2013) Inhibition of inhibition in visual
1092 cortex: the logic of connections between molecularly distinct interneurons. *Nat Neurosci*
1093 16:1068-1076.

1094 Pho GN, Goard MJ, Woodson J, Crawford B, Sur M (2018) Task-dependent representations of
1095 stimulus and choice in mouse parietal cortex. *Nat Commun* 9:2596.

1096 Pinto L, Dan Y (2015) Cell-Type-Specific Activity in Prefrontal Cortex during Goal-Directed
1097 Behavior. *Neuron* 87:437-450.

1098 Pnevmatikakis EA, Soudry D, Gao Y, Machado TA, Merel J, Pfau D, Reardon T, Mu Y,
1099 Lacefield C, Yang W, Ahrens M, Bruno R, Jessell TM, Peterka DS, Yuste R, Paninski L

1100 (2016) Simultaneous Denoising, Deconvolution, and Demixing of Calcium Imaging
1101 Data. *Neuron* 89:285-299.

1102 Poort J, Khan AG, Pachitariu M, Nemri A, Orsolic I, Krupic J, Bauza M, Sahani M, Keller GB,
1103 Mrsic-Flogel TD, Hofer SB (2015) Learning Enhances Sensory and Multiple Non-
1104 sensory Representations in Primary Visual Cortex. *Neuron* 86:1478-1490.

1105 Raposo D, Kaufman MT, Churchland AK (2014) A category-free neural population supports
1106 evolving demands during decision-making. *Nat Neurosci* 17:1784-1792.

1107 Ringach DL, Mineault PJ, Tring E, Olivas ND, Garcia-Junco-Clemente P, Trachtenberg JT
1108 (2016) Spatial clustering of tuning in mouse primary visual cortex. *Nat Commun*
1109 7:12270.

1110 Rudy B, Fishell G, Lee S, Hjerling-Leffler J (2011) Three groups of interneurons account for
1111 nearly 100% of neocortical GABAergic neurons. *Dev Neurobiol* 71:45-61.

1112 Ruebel O et al. (2019) NWB:N 2.0: An Accessible Data Standard for Neurophysiology. *bioRxiv*.

1113 Runyan CA, Piasini E, Panzeri S, Harvey CD (2017) Distinct timescales of population coding
1114 across cortex. *Nature* 548:92-96.

1115 Runyan CA, Schummers J, Van Wart A, Kuhlman SJ, Wilson NR, Huang ZJ, Sur M (2010)
1116 Response features of parvalbumin-expressing interneurons suggest precise roles for
1117 subtypes of inhibition in visual cortex. *Neuron* 67:847-857.

1118 Rustichini A, Padoa-Schioppa C (2015) A neuro-computational model of economic decisions. *J*
1119 *Neurophysiol* 114:1382-1398.

1120 Sahara S, Yanagawa Y, O'Leary DD, Stevens CF (2012) The fraction of cortical GABAergic
1121 neurons is constant from near the start of cortical neurogenesis to adulthood. *J Neurosci*
1122 32:4755-4761.

1123 Schoups A, Vogels R, Qian N, Orban G (2001) Practising orientation identification improves
1124 orientation coding in V1 neurons. *Nature* 412:549-553.

1125 Sohya K, Kameyama K, Yanagawa Y, Obata K, Tsumoto T (2007) GABAergic neurons are less
1126 selective to stimulus orientation than excitatory neurons in layer II/III of visual cortex, as
1127 revealed by in vivo functional Ca²⁺ imaging in transgenic mice. *J Neurosci* 27:2145-
1128 2149.

1129 Song YH, Kim JH, Jeong HW, Choi I, Jeong D, Kim K, Lee SH (2017) A Neural Circuit for
1130 Auditory Dominance over Visual Perception. *Neuron* 93:940-954 e946.

1131 Taniguchi H, He M, Wu P, Kim S, Paik R, Sugino K, Kvitsiani D, Fu Y, Lu J, Lin Y, Miyoshi
1132 G, Shima Y, Fishell G, Nelson SB, Huang ZJ (2011) A resource of Cre driver lines for
1133 genetic targeting of GABAergic neurons in cerebral cortex. *Neuron* 71:995-1013.

1134 Tanimoto N, Sothilingam V, Kondo M, Biel M, Humphries P, Seeliger MW (2015)
1135 Electroretinographic assessment of rod- and cone-mediated bipolar cell pathways using
1136 flicker stimuli in mice. *Sci Rep* 5:10731.

1137 Teeters JL et al. (2015) Neurodata Without Borders: Creating a Common Data Format for
1138 Neurophysiology. *Neuron* 88:629-634.

1139 Thomson AM, Lamy C (2007) Functional maps of neocortical local circuitry. *Front Neurosci*
1140 1:19-42.

1141 Viswanathan P, Nieder A (2015) Differential impact of behavioral relevance on quantity coding
1142 in primate frontal and parietal neurons. *Curr Biol* 25:1259-1269.

1143 Vogelstein JT, Packer AM, Machado TA, Sippy T, Babadi B, Yuste R, Paninski L (2010) Fast
1144 nonnegative deconvolution for spike train inference from population calcium imaging. *J*
1145 *Neurophysiol* 104:3691-3704.

1146 Wang XJ (2002) Probabilistic decision making by slow reverberation in cortical circuits. *Neuron*
1147 36:955-968.

1148 Wang XJ, Yang GR (2018) A disinhibitory circuit motif and flexible information routing in the
1149 brain. *Curr Opin Neurobiol* 49:75-83.

1150 Wang XJ, Tegner J, Constantinidis C, Goldman-Rakic PS (2004) Division of labor among
1151 distinct subtypes of inhibitory neurons in a cortical microcircuit of working memory.
1152 *Proc Natl Acad Sci U S A* 101:1368-1373.

1153 Wong KF, Wang XJ (2006) A recurrent network mechanism of time integration in perceptual
1154 decisions. *J Neurosci* 26:1314-1328.

1155 Yoshimura Y, Callaway EM (2005) Fine-scale specificity of cortical networks depends on
1156 inhibitory cell type and connectivity. *Nat Neurosci* 8:1552-1559.

1157 Yoshimura Y, Dantzker JL, Callaway EM (2005) Excitatory cortical neurons form fine-scale
1158 functional networks. *Nature* 433:868-873.

1159 Zhong L, Zhang Y, Duan CA, Pan J, Xu N-l (2018) Dynamic and causal contribution of parietal
1160 circuits to perceptual decisions during category learning. *bioRxiv*.

1161 Znamenskiy P, Kim M-H, Muir DR, Iacaruso MF, Hofer SB, Mrsic-Flogel TD (2018) Functional
1162 selectivity and specific connectivity of inhibitory neurons in primary visual cortex.
1163 *bioRxiv*.